Astron. Astrophys. 156, 354–380 (1986)

ASTRONOMY
AND
ASTROPHYSICS

Computation of the quasi-steady gas flow in a spiral galaxy by means of a multigrid method

W. A. Mulder*

Sterrewacht, Huygens Laboratorium, P.O. Box 9513, NL-2300 RA Leiden, The Netherlands

Received February 4, accepted August 20, 1985

Summary. An efficient numerical method for the integration of the Euler equations for gas dynamics is presented. The key assumption is the existence of a stationary solution. The several elements of the method, most of which have been described elsewhere, are reviewed in some detail to provide a reference in the astronomical literature and to promote its use in astrophysics.

The equations are discretized in space by means of upwind differencing through flux-vector splitting. This allows for the crisp representation of shocks. The time-integration is carried out by an implicit scheme. The linear system that arises in the implicit formulation is solved efficiently by a multigrid correction scheme, using symmetric line/Gauss-Seidel relaxation.

The method is applied to the well-studied problem of the quasi-steady isothermal gas flow in the gravitational potential of a weakly barred galaxy. Convergence on a 64×64 grid typically takes 100 to 300 multigrid cycles for a second-order-accurate solution. Comparison with first-order-accurate solutions shows that second-order schemes are to be preferred, despite their slower convergence.

There are two fundamentally different types of quasi-steady solutions, depending on the strength of the bar and the size of the sound speed. Type I has only shocks inside co-rotation. The dissipation in these shocks causes a net average inflow. A quasi-steady solution is obtained by keeping the central density fixed. The inflow rate turns out to be very small, of the order of the numerical discretization error. The solution is practically independent of the actual value of the central density. The torque between the bar and the gas has an associated timescale much larger than the Hubble time. These results validate the quasi-steady approach. On the other hand, the small magnitude of the inflow rate indicates that the inflow in a real galaxy is likely to be determined by processes other than dissipation in shocks.

Type II solutions have shocks inside and outside co-rotation. The first cause inflow and the latter outflow, thus depleting the region around co-rotation and creating two rings, one at a radius well within the ILR and one at a radius beyond the OLR. A quasi-steady solution is obtained by adding gas in depleted regions and removing it from high-density regions.

The solutions display strong non-circular motions. It is suggested that the tilted-ring model for the observed neutral-hydrogen velocity field of disk galaxies may just as well be interpreted as a rotated-ellipse model. A set of edge-on rotation curves is presented that can be compared with those based on neutral-hydrogen observations. They show that the assumption of circular motion for the interpretation of observed rotation curves can be misleading.

Key words: barred galaxies – kinematics and dynamics of galaxies – hydrodynamics – numerical methods – shock waves

1. Introduction

A large class of evolutionary problems can be described by a set of hyperbolic partial differential equations. These appear, e.g., in aerodynamics, biology, chemistry, econometrics and, of course, astronomy. An important subset is formed by those problems where one is not interested in the actual evolutionary behaviour, but only in a steady state that can be reached asymptotically. Whereas the numerical time-integration of hyperbolic equations may require excessive computer resources, the pursuit of a stationary solution allows for substantial short-cuts. Some recent advancements in this field can be found in a series of earlier papers (Paper I: Mulder and van Leer, 1985; Paper II: van Leer and Mulder, 1985; Paper III: Mulder, 1985b). There, the development of an efficient and powerful method for computing steady solutions of the Euler equations for gas dynamics is described.

The motivation for the work presented in this paper is twofold. In the first place, we want to test the method on a difficult but well-studied problem: the quasi-steady flow of isothermal gas in a disk galaxy. Secondly, the availability of the code allows for the relatively fast computation of accurate solutions. These can be used to model the observed velocity fields in spiral galaxies.

It is well known that a non-axisymmetric perturbation like a spiral density wave or an oval distortion creates a spiral pattern of shocks in a gaseous disk. Computations of this response problem by a one-dimensional approximation can be found in papers by Fujimoto (1968), Roberts (1969), and Woodward (1975) for a gravitational potential with a spiral density wave, and by Roberts et al. (1979) for a barred potential. Fully two-dimensional computations have been carried out by Sørenson et al. (1976), Sanders and Huntley (1976), Sanders and Tubbs (1980), van Albada and Roberts (1981), Sørensen and Matsuda (1982), Schempp (1982), and van Albada (1985). The self-gravity of the gas is included by Berman et al. (1979) and Huntley (1980). Although the results roughly agree in a qualitative sense, large quantitative differences arise. The lack of numerical accuracy of some of the numerical schemes causes details to be smeared out and mixes numerical with physical effects. This may lead to ambiguous conclusions concerning the global transport properties and timescales. Accurate time-dependent numerical solutions have been presented by van Albada and Roberts (1981) and van Albada (1985).

* Present address: Dept. of Computer Science, Stanford University, Stanford, CA 94305, USA

The quality of a numerical solution to a steady problem can be characterized by two types of errors: (i) the spatial discretization error, and (ii) the deviation from the steady state. The first type originates in the *spatial* representation of the flow by a finite set of state quantities on a grid. The local discretization error is defined as the difference between the numerical and the exact value of a state quantity at a given position. If a two-dimensional problem is treated on a square Cartesian grid with cell size $\Delta x = \Delta y$, then the discretization error is proportional to $(\Delta x)^s$. Most schemes are first-order-accurate ($s=1$). Differences in accuracy arise from the constant of proportionality, which may strongly vary among several schemes. Second-order schemes have $s=2$ and can provide a very good accuracy even on medium-sized grids. A general method for the construction of higher-order schemes has been invented by van Leer (1977). A second-order scheme in combination with flux-vector splitting (van Leer, 1982) has been shown to yield good results (van Albada et al., 1982; van Albada, 1985). It will be used in this paper as well. It should be remarked, however, that the method is second-order-accurate only in smooth regions of the flow, so formally it should not bear this name. Nevertheless, the improvement in accuracy with respect to a first-order scheme is so large that the name will be used anyhow.

The second type of error is the deviation from the steady state and is associated with the discrete *temporal* representation of the state quantities. It is represented by the so-called residual, a term which either refers to the local time-derivative or to its global norm. Deviations from the correct numerical steady state remain if the time-integration is stopped too early, or if the integration scheme is unable to bring down the residual well below the level of the discretization error.

The above distinction between spatial and temporal errors is appropriate for most methods designed uniquely for finding steady solutions. It is, of course, possible to use time-accurate methods in marching towards the steady state. Although this is far from efficient, it is often done because of the more general availability of time-accurate codes. In some of these schemes, the residual depends explicitly on the size of the timestep. Then, the spatial and temporal errors cannot be clearly separated. An example is the second-order-accurate scheme described by van Albada et al. (1982). A comparison between their one-dimensional steady solution and the one obtained in Paper I reveals no noticeable differences in spatial accuracy, implying that the dependence of the residual on the timestep does not matter in this case. For two-dimensional steady problems, the use of time-splitting may worsen the effect of a timestep-dependent residual.

The method described in this paper is designed to quickly bring down the residual to a desired level. In this way only the spatial discretization error remains. A prerequisite is the existence of a steady or quasi-steady solution.

Section 2 of this paper describes the problem of determining the quasi-steady flow in a disk galaxy. Spiral structure is generated by an oval distortion or weak bar. Some general properties of the solution are reviewed.

The numerical scheme is described in Sect. 3. First, the discretization in space is described. The numerical representation of the state quantities is constructed in such a way that the numerical solution for the axisymmetric case *exactly* equals the analytical solution. Then the method for finding the steady state is discussed. It is a mixture of time-accurate integration by means of an implicit scheme and relaxation by Newton's method. A multigrid correction scheme is used to solve the large linear system that arises in this method. The basic principles can be found in the earlier Papers I, II, and III. The various ingredients of the method are reviewed here to provide a reference in the astronomical literature and to promote its use in astrophysics. The method is spelled out for the isothermal Euler equations, but is equally applicable to the non-isothermal Euler equations (cf. Papers II and III). Some fundamental improvements are added in this paper. First, the timestep is based on a local rather than a global value (Sect. 3.2). Secondly, the timestep is used in the relaxation scheme, but not in the linear updates during the multigrid cycle (Sect. 3.3). Thirdly, an approximate linearization for the second-order-accurate spatial discretization is introduced that has the same structure as in the first-order-accurate scheme, but preserves the homogeneity of the equations (Appendix II).

Numerical results are presented in Sect. 4. The parameters that determine the quasi-steady solution are given in Sect. 4.1. The computational efficiency of the multigrid method is investigated in Sect. 4.2. The global properties of the quasi-steady solutions are considered in Sect. 4.3. The spiral pattern and velocity field are discussed in Sect. 4.4. Finally, edge-on rotation curves are presented in Sect. 4.5.

Section 5 contains some concluding remarks and summarizes the main results of this paper.

2. The problem

2.1. The isothermal Euler equations

In this paper the gaseous components of the interstellar medium are described by the two-dimensional inviscid Euler equations. The basic assumptions that lead to this choice will be briefly reviewed (Shu et al., 1972).

First, the timescales for thermal balance are relatively short, so that the effective temperature of the ISM may be taken constant. Secondly, most of the gas is confined to a thin layer. If the state quantities of the gas are averaged over the thickness of the layer, the three-dimensional equations reduce to a two-dimensional set. Thirdly, the various components of the ISM are modelled by an ideal gas with negligible viscosity. In addition, the self-gravity of the gas is ignored.

Consider a galactic potential $V(R,\phi)$ rotating with a pattern speed ω. The equations describing the flow of isothermal gas in the co-rotating frame are

$$\frac{\partial w}{\partial t} = s(w) - \frac{\partial f(w)}{\partial R} - \frac{\partial g(w)}{\partial \phi}. \tag{1}$$

Here w represents the vector of conserved state quantities, $f(w)$ and $g(w)$ are the fluxes in the R- and ϕ-direction, respectively, and $s(w)$ is the source term. If ϱ is the local density and u and v are the velocities in the R- and ϕ-direction, then

$$w = R\varrho \begin{pmatrix} 1 \\ u \\ v \end{pmatrix}, \quad f = R\varrho \begin{pmatrix} u \\ u^2+c^2 \\ uv \end{pmatrix}, \quad g = \varrho \begin{pmatrix} v \\ uv \\ v^2+c^2 \end{pmatrix}$$

and

$$s = \varrho \begin{pmatrix} 0 \\ -R\dfrac{\partial V}{\partial R} + c^2 + (v+\omega R)^2 \\ -\dfrac{\partial V}{\partial \phi} - u(v+2\omega R) \end{pmatrix}. \tag{2}$$

The integral form of Eq. (1) is

$$\frac{\partial}{\partial t}\int\int_S dR d\phi w = \int\int_S dR d\phi s - \oint_{\partial S}(f d\phi - g dR) \tag{3}$$

for a domain S with boundary ∂S. The Euler equations in this conservation form allow for discontinuous or *weak* solutions. It should be kept in mind that the Euler equations represent the limit for zero viscosity of the full Navier-Stokes equations. If one simply sets the viscosity to zero in the latter, solutions with shocks where energy is created instead of dissipated, are formally allowed. To exclude these unphysical solutions an *entropy condition* has to be specified in addition to (3) which states that energy is always dissipated or at least conserved. This condition is automatically fulfilled by a proper numerical scheme (Harten et al., 1981).

2.2. The gravitational potential

The potential used in the numerical computations is a two-dimensional version of the one given by Mulder and Hooimeyer (1984, Paper IV hereafter). It corresponds to a triaxial power-law distribution of gravitating matter (the gravity of the gas will be neglected throughout):

$$\varrho^* = \varrho_0^* m^p,$$

with

$$m^2 = (x/a)^2 + (y/b)^2 + (z/c)^2. \tag{4}$$

This expression is written in spherical coordinates and expanded in spherical harmonics. The potential is found by simple quadratures. A weighting function suppresses the ϕ-dependence outside a given radius. In this way, a weak bar in an oblate halo can be obtained (see Appendix I of Paper IV).

The power p is chosen to be -1.8, in agreement with observations of the galactic bulge (Sanders and Lowinger, 1972; Isaacman, 1981) and measured rotation curves of Sc galaxies (Burstein et al., 1982) and Sb galaxies (Rubin et al., 1982). The axisymmetric rotation curve, corresponding to this value, is

$$v_{\rm rot} \propto r^{1+\frac{1}{2}p}, \tag{5}$$

where $1+\frac{1}{2}p = 0.1$ for our choice. This type of rotation curve is very steep near the centre and almost flat at large radii.

The other parameters that define the potential are: the axial ratios b/a and c/a of the intermediate and short axis with respect to the long axis, and the radius where the bar ends. The axial ratio c/a of the short to the long axis has no meaning in the two-dimensional case. It is set to 0.5 when the constants for the potential are computed. The ratio b/a is left as a free parameter and will be specified in Sect. 4.1. The parameters describing the weighting function are identical to those in Paper IV.

Dimensionless units are defined by $r_0 = a = 1$ as the unit of length and $v_0 = r_0(4\pi G\varrho_0^*)^{1/2} = 1$ as the unit of velocity.

The potential in the plane $z=0$ is

$$V(R,\phi) = R^{p+2}\{c_0 + c_2(R)\cos(2\phi)\}, \tag{6}$$

where $R = (x^2+y^2)^{1/2}$. The higher-order terms of the expansion in spherical harmonics have been neglected. The constant c_0 is related to the constants c_{nm} of Appendix I in Paper IV: $c_0 = c_{00} - \frac{1}{2}c_{20} + \frac{3}{8}c_{40}$, up to $n=4$. The function $c_2(R) = 3c_{22}(R)$ can be found in the same appendix. If there is no cut-off of the bar, $c_2(R)$ is a constant.

2.3. The steady state

The aim of the present paper is to find a stationary solution of Eq. (3). However, the existence of such a solution is not immediately clear. In this and the next two paragraphs we consider the conditions under which a steady state can be reached.

Equation (3) can be written in a more transparent form by the introduction of the total time-derivative along a streamline:

$$\frac{d}{dt} = \frac{\partial}{\partial t} + u\frac{\partial}{\partial R} + \frac{v}{R}\frac{\partial}{\partial \phi}. \tag{7}$$

The result is

$$\frac{d\ln\varrho}{dt} = -\frac{1}{R}\frac{\partial(Ru)}{\partial R} - \frac{1}{R}\frac{\partial v}{\partial \phi}, \tag{8a}$$

$$\frac{du}{dt} = -\frac{\partial}{\partial R}(V + c^2\ln\varrho) + (v+\omega R)^2/R \tag{8b}$$

$$\frac{dv}{dt} = -\frac{1}{R}\frac{\partial}{\partial \phi}(V + c^2\ln\varrho) - u(v+2\omega R)/R. \tag{8c}$$

If Eq. (8b) is multiplied by u and Eq. (8c) by v, it is found after addition that

$$\frac{dH}{dt} = \frac{\partial}{\partial t}(c^2\ln\varrho),$$

with

$$H = \tfrac{1}{2}(u^2+v^2) - \tfrac{1}{2}\omega^2R^2 + V(R,\phi) + c^2\ln\varrho. \tag{9}$$

Consequently, the "integral" H is constant on a streamline in the stationary case (H is Bernoulli's constant). In the presence of shocks this is not true any more, as shown by Roberts et al. (1972). At a shock there is a jump in H, caused by dissipation. If u_1 is the velocity perpendicular and u_2 parallel to the shock, then u and v can be transformed in u_1 and u_2 by a local rotation of the coordinate frame. The pre- and postshock state are related by the jump equations for a steady shock:

$$\begin{aligned} \varrho_L u_{1L} &= \varrho_R u_{1R}, \\ \varrho_L(u_{1L}^2 + c^2) &= \varrho_R(u_{1R}^2 + c^2), \\ u_{2L} &= u_{2R}, \end{aligned} \tag{10}$$

where L denotes the preshock and R the postshock values. The entropy condition can be satisfied by the additional requirement that u_{1L} is supersonic and u_{1R} subsonic. From Eq. (10) it follows that $M_{1L} = 1/M_{1R}$ and $\varrho_L = \varrho_R M_{1R}^2$, where the mach number $M_1 \equiv u_1/c$. The jump in H becomes

$$H_R - H_L = -c^2\{(1-M_{1R}^4)/M_{1R}^2 + \ln M_{1R}^2\}, \tag{11}$$

which is always negative since $|M_{1R}| < 1$. The obvious conclusion is that streamlines are not closed, so there must be a net inflow or outflow in the presence of shocks.

A solution with a non-zero inflow or outflow clearly cannot be stationary. But if we only consider a domain S given by $R_{\min} \leqq R \leqq R_{\max}$ and $0 \leqq \phi \leqq 2\pi$ and neglect the evolution of the flow outside S, the flow inside the domain may become steady. This type of solution will be called *quasi-stationary*.

2.4. The axisymmetric case

More insight in the quasi-stationary state can be obtained if the axisymmetric case is considered. The equations then can be solved

analytically. In the absence of shocks Eqs. (8a–c) can be replaced by

$$w_2 = R\varrho u = \text{const}, \tag{12a}$$

$$\frac{du}{dt} = J^2/R^3 - \frac{\partial}{\partial R}(V_0 + c^2 \ln \varrho), \tag{12b}$$

$$\frac{dJ}{dt} = 0, \tag{12c}$$

where we have introduced the angular momentum $J = R(v + \omega R)$. The axisymmetric part of the potential in Eq. (6) is denoted by $V_0 = c_0 R^{p+2}$. An obvious stationary solution is

$$w_2 = 0, \quad \varrho = \varrho_0, \quad u = 0, \quad J = \omega_0 R^2$$

with

$$\omega_0^2 = \frac{1}{R}\frac{\partial V_0}{\partial R}. \tag{13}$$

Every streamline now is a circle with its own value of J (and H). The rotation curve becomes

$$v_{\text{rot}} = v + \omega R = J/R = \omega_0 R = [(p+2)c_0]^{1/2} R^{1+\frac{1}{2}p}, \tag{14}$$

in agreement with Eq. (5).

If $w_2 \neq 0$ this situation changes drastically. A streamline now covers the whole domain S. On the streamline both J and H are conserved, where

$$H = \tfrac{1}{2}((w_2/\varrho R)^2 + (J/R)^2) - \omega J + V_0(R) + c^2 \ln \varrho. \tag{15}$$

The quantities ϱ, u, and v follow from w_2, J, and H. The rotation curve is $v_{\text{rot}} \propto R^{-1}$, which is not quite what we would like to have. The density can be found approximately by expansion around a fixed radius R_0. Let J and H be computed at R_0 according to (14) and (15), assume w_2 to be very small, and define $x \equiv R - R_0$. Then

$$\varrho \simeq \varrho_0 \exp(-\tfrac{1}{2}\omega_1^2 x^2/c^2), \quad \text{where} \quad \omega_1^2 = 3\omega_0^2 + \frac{\partial^2 V_0}{\partial R^2}. \tag{16}$$

The epicycle frequency $\omega_1 = (p+4)^{1/2}\omega_0$ for our potential and is of order unity, whereas c is at least an order of magnitude smaller. The width c/ω_1 of the Gaussian density distribution (16) is consequently fairly small, implying that most of the gas is concentrated in a ring around R_0. We thus have the odd situation that an arbitrary small deviation from zero inflow or outflow results in a totally different stationary solution. Although the timescale required to reach such a steady state may be unacceptably large for very small w_2, it would be better if we had a smooth transition between the solutions for zero and non-zero w_2. The answer lies in the fact that the Euler equations are the limit for zero viscosity of the full viscous equations. We will therefore continue with the latter.

The viscous equations for the axisymmetric case are

$$\frac{\partial}{\partial t}(R\varrho) + \frac{\partial}{\partial R}(R\varrho u) = 0, \tag{17a}$$

$$\frac{\partial u}{\partial t} + u\frac{\partial u}{\partial R} = \left(J^2/R^3 - \frac{\partial V}{\partial R}\right) - \frac{c^2}{\varrho}\frac{\partial \varrho}{\partial R} + \frac{(\lambda + \frac{4}{3}\mu)}{\varrho}\frac{\partial}{\partial R}\frac{1}{R}\frac{\partial}{\partial R}(Ru), \tag{17b}$$

$$\frac{\partial J}{\partial t} + u\frac{\partial J}{\partial R} = \frac{R\mu}{\varrho}\frac{\partial}{\partial R}\frac{1}{R}\frac{\partial J}{\partial R}. \tag{17c}$$

Here μ and λ are the coefficients of shear and bulk viscosity, respectively. Both are positive. The steady solution of (17a) is $w_2 = R\varrho u = \text{const}$. This can be used to simplify Eq. (17c), which results in the solution

$$J = J_0 + J_1 R^{2 + w_2/\mu}, \tag{18}$$

where J_0 and J_1 are constants. For $J_1 = 0$ we obtain the previous inviscid solution for $w_2 \neq 0$. But if it is assumed that $w_2 = \frac{1}{2}p\mu$, the proper rotation curve can be obtained for $J_0 = 0$ and $J_1 = \{(p+2)c_0\}^{1/2}$. Because p is negative, w_2 is negative as well, which implies *inflow*. Furthermore, this inflow is proportional to the coefficient of shear viscosity. The limit for vanishing viscosity still gives the proper rotation curve, as desired.

If it is assumed that the angular momentum J balances the potential, as in Eq. (13), then Eq. (17b) becomes in the steady case

$$y^2\frac{d^2y}{dx^2} + \beta(y^2 - 1)\frac{dy}{dx} - (y^2 + \beta)y = 0. \tag{19}$$

Here $y = -u/c$, $x = \ln R$, and $\beta = -w_2/(\lambda + \frac{4}{3}\mu)$. A solution of (19) in general contains shocks, but at the moment we are only interested in a solution for small y. An approximate solution for $y \ll 1$ is $y \propto e^{-x} = 1/R$. Through $w_2 = R\varrho u$ it follows that the density is independent of R. Thus, a steady solution of the viscous equations in the axisymmetric case is

$$\varrho = \varrho_0, \quad u = w_2/(R\varrho_0), \quad J = \{(p+2)c_0\}^{1/2} R^{2 + w_2/\mu} = \omega_0 R^2, \quad w_2 = \tfrac{1}{2}p\mu < 0. \tag{20}$$

This solution gives a smooth transition to (13) for a vanishing coefficient of shear viscosity μ. The earlier solution with $v_{\text{rot}} \propto R^{-1}$ and ϱ according to (16) is hereby avoided.

The solution (20) can serve as the initial condition for the numerical computations, with w_2 set to zero. It also describes the flow in regions where the influence of the bar or oval distortion is small.

2.5. *The general case*

The occurrence of shocks in the non-axisymmetric case causes a net inflow or outflow, as mentioned in Sect. 2.3. To determine the sign of this flow at a certain radius, we assume the deviations from axisymmetry to be small. The dominant part of the tangential velocity then is $v \simeq (\omega_0 - \omega)R$, with ω_0 as defined in Eq. (13), whereas $u \simeq 0$ and $\varrho \simeq \varrho_0$. For $\varrho_0 = 1$, the constant H becomes

$$H \simeq \tfrac{1}{2}(\omega_0^2 - 2\omega\omega_0)R^2 + V_0(R). \tag{21}$$

The derivative of H with respect to R is

$$\frac{dH}{dR} \simeq \tfrac{1}{2}\omega_1^2/\omega_0(\omega_0 - \omega)R \simeq \frac{\Delta H}{\Delta R}. \tag{22}$$

The factor $\omega_0 - \omega$ is positive inside and negative outside co-rotation. A negative jump ΔH will therefore cause inflow inside and outflow outside co-rotation.

We now may distinguish two types of solutions. Type I only has shocks inside co-rotation (CR). There is a net inflow. The solution outside CR can approximately be described by Eq. (20), apart from periodic terms. The shocks pump gas from this reservoir towards the centre, where it will accumulate in a region without shocks. From the equation of continuity, the first of (3), it follows that the average inflow per ring is constant throughout the entire domain S (as defined at the end of Sect. 2.3):

$$\langle w_2 \rangle \equiv \frac{1}{2\pi}\int_0^{2\pi} d\phi\, w_2(R, \phi) = \text{const}. \tag{23}$$

This results holds even in the presence of shocks. As long as $\langle w_2 \rangle$ is small, the evolution outside the domain S indeed may be neglected.

Far outside CR, where the Type I solution is practically axisymmetric, the actual value of $\langle w_2 \rangle$ will be determined by the coefficient of shear viscosity μ. Formally, the Euler equations are inviscid and this coefficient vanishes. In practice, the representation of the state quantities on a grid with finite cell size introduces a discretization error that has the effect of a viscous term. Consequently, the actual value of $\langle w_2 \rangle$ in the numerical solution far outside CR will be determined by the coefficient of numerical viscosity μ_{num}. In the region of shocks, the dissipation in shocks will effectively increase the viscosity, to which the solution will adapt itself while keeping $\langle w_2 \rangle$ constant. We conclude that an exact solution of the inviscid Euler equations in case of a type I galaxy is expected to be physically irrelevant. Viscosity should be added explicitly, i.e., the full Navier-Stokes equations should be solved. However, as long as the numerical viscosity is larger than the physical viscosity, the explicit viscous terms can better be left out to avoid the excessive smearing of details. Only on very fine grids the addition of these terms will become necessary.

The second type of solution has shocks inside and outside co-rotation. This Type II cannot be stationary, as the shocks inside CR pump gas towards the centre and the shocks outside CR pump the gas outward, to the end of the shocks, which usually will be at a radius somewhere outside the Outer Lindblad Resonance (OLR). At that point a ring like the one described by Eq. (16) may be formed. Near the Inner Lindblad Resonance (our potential has only one ILR) a similar ring will be created. A steady solution can be obtained by the introduction of an additional source-term that creates mass in highly depleted regions. One might think of mass loss by stars and infall of intergalactic matter. Also the thin-disk assumption may break down in this case, thus affecting the global transport properties of the system. As ring-like structures are observed anyhow, the use of a time-dependent integration-scheme is more appropriate in this case. Van Albada (1985) has shown that the timescale for significant depletion in the case of a weak bar is well above the 5 Gyr. As we still would like to use our computer program for this kind of solution, we simply introduce an additional source term for mass-creation and -loss (van Albada, private communication):

$$s_M = RM(\varrho)\begin{pmatrix} 1 \\ u_p \\ v_p \end{pmatrix}, \quad \text{with} \quad M(\varrho) = \alpha_M(\varrho_0 - \varrho). \tag{24}$$

Here α_M is a small positive parameter, to be specified later. If the local density is smaller than ϱ_0, gas is added; if it is larger, material is removed. The velocities u_p and v_p are the prescribed velocities of the matter that is added or removed. As most of the gas is driven away from the region around CR, we favour this region by letting $u_p = v_p = 0$. (Alternatively, one may adopt the local velocity of the gas, i.e., $u_p = u$ and $v_p = v$; this choice will not be considered here.) The source term (24) is added to the right-hand side of Eq. (1), and in the equations derived from this one. Now a steady state can be attained.

The validity of a quasi-steady solution, once obtained, can be judged by estimating the timescales of the suppressed unsteady processes. For a Type I solution this requires the evaluation of the average inflow rate and of the dependence on the numerical viscosity. In addition, the change of angular momentum of the bar should be considered. The bar exerts a torque on the gas and causes a change in its total angular momentum:

$$\frac{dL_{\text{gas}}}{dt} = -\int_{R_{\min}}^{R_{\max}} dR \int_0^{2\pi} d\phi R\varrho \frac{\partial V}{\partial \phi}, \tag{25a}$$

where

$$L_{\text{gas}} = \int_{R_{\min}}^{R_{\max}} dR \int_0^{2\pi} d\phi R\varrho J. \tag{25b}$$

Conservation of angular momentum implies $dL_{\text{gas}}/dt = -dL_{\text{bar}}/dt$. The timescale associated with this process is

$$\tau_{\text{bar}} = \frac{L_{\text{bar}}}{|dL_{\text{bar}}/dt|}. \tag{26}$$

Because we do not have a self-consistent model for the bar, the total angular momentum of the bar L_{bar} can only be estimated. The work by Pfenniger (1984) shows that the assumption of solid-body rotation provides a reasonable value. If the bar ends at a radius R_{co} and has a pattern speed ω, we can derive (using formulae in Paper IV):

$$\begin{aligned} L_{\text{bar}} &= \frac{(4\pi G\varrho_0^*)}{G}\tilde{L}_{\text{bar}}, \\ \tilde{L}_{\text{bar}} &= \frac{8}{5}\omega a_{22}\frac{2i^2}{(p+5)(p+5+i)(p+5+2i)}R_{\text{co}}^{p+5}. \end{aligned} \tag{27}$$

Here G is the constant of gravity. The definition of model units implies $4\pi G\varrho_0^* = 1$. The constant i originates from the weighting function that cuts off the bar at R_{co}; we use $i = 10$ here. The constant a_{22} is related to $c_2(0) = 3c_{22}(0)$ by $a_{22} = p(p+5)c_{22}(0)$. The timescale that describes the substantial gain or loss of angular momentum of the bar

$$\tau_{\text{bar}} = 0.226\frac{\tilde{L}_{\text{bar}}}{|dL_{\text{gas}}/dt|}\frac{v_0(\text{km/s})}{\varrho_0(M_\odot/\text{pc}^2)}\text{Gyr}. \tag{28}$$

Here v_0 is the model unit of velocity and ϱ_0 the unit of surface density for the gas.

For a Type II solution, Eq. (23) does not hold any more. We expect $\langle w_2 \rangle$ to be negative inside and positive outside CR. The actual size of $\langle w_2 \rangle$ will depend on α_M. Equation (24), in combination with (1) and (2), shows that α_M^{-1} has the dimension of time. The timescale corresponding with the source term (24) can therefore be estimated by

$$\tau_M = \alpha_M^{-1}, \tag{29}$$

expressed in the model unit of time r_0/v_0. The timescale τ_{bar}, as described above for a Type I solution, is equally applicable to a Type II solution.

We now have a qualitative impression of the quasi-steady solutions, and can judge their validity by evaluating the timescales of the suppressed unsteady processes. Before presenting the results, a fairly technical description of the numerical method will be given in the next section. This may be skipped by the reader who in not interested in numerical techniques.

3. Numerical method

3.1. *Spatial discretization*

The discretization in space of the Euler equations involves the formulation of a large set of simultaneous finite-difference equations that mimic the continuum equations reasonably well on a grid with finite cell size. The numerical solution should approach the solution of the continuum equations in the limit of vanishing cell size. In this paragraph the discretization in space of the right-hand side of Eq. (3) will be discussed.

Let the computational domain S cover a region with R between $R_{\min}$ and $R_{\max}$ and ϕ between 0 and π. The symmetry of the problem requires only one halfplane. The domain is divided in $N=N_R\times N_\phi$ cells. The grid has a constant spacing $\Delta\phi=\pi/N_\phi$ in the ϕ-direction. The R-grid is stretched in such a way that $\xi=R^{1+\kappa}$ is equidistant: $\Delta\xi=(R_{\max}^{1+\kappa}-R_{\min}^{1+\kappa})/N_R$. For $\kappa=0$ we have an equidistant grid in R, for $\kappa=p/2$ the rotation curve (14) has a constant derivative with respect to ξ. The latter option will be used for the numerical examples in Sect. 4. A cell will be denoted by indices i and j for the ϕ- and R-direction, respectively, with $i=1,\ldots,N_\phi$ and $j=1,\ldots,N_R$. The centre of a cell is labelled by (i,j), the interfaces by $(i\pm\frac{1}{2},j)$ or $(i,j\pm\frac{1}{2})$. The gridsize in R can now be written as $\Delta_jR=R_{j+\frac{1}{2}}-R_{j-\frac{1}{2}}$. Here $R_{j+\frac{1}{2}}=\xi_{j+\frac{1}{2}}^{1/(1+\kappa)}$ and $\xi_{j+\frac{1}{2}}=R_{\min}^{1+\kappa}+j\Delta\xi$. The centre of a cell is positioned at a radius $R_j=\frac{1}{2}(R_{j-\frac{1}{2}}+R_{j+\frac{1}{2}})$ and angle $\phi_i=\frac{1}{2}(\phi_{i-\frac{1}{2}}+\phi_{i+\frac{1}{2}})$, where $\phi_{i+\frac{1}{2}}=i\Delta\phi$.

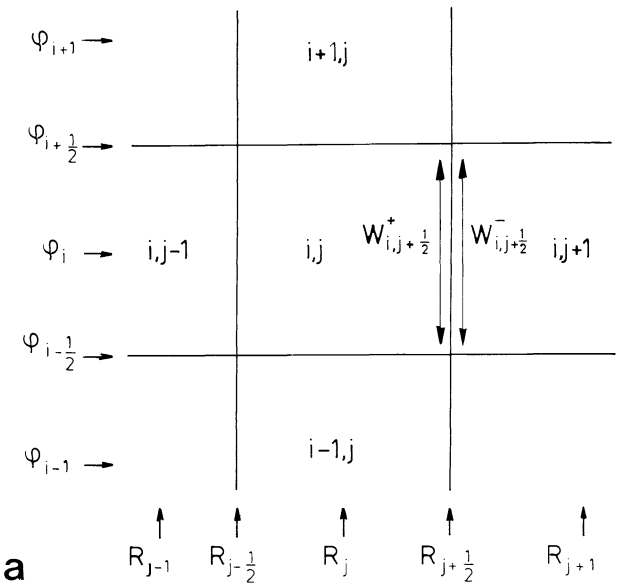

Fig. 1a. Geometry of the computational domain, showing the positions of the various quantities defined in Sect. 3.1. The lines of constant R and ϕ are indicated by small arrows. The ϕ-grid is equidistant, the R-grid is not. The state quantities w_{ij} are defined as cell averages, the line average at the left side of the interface $(i,j+1/2)$ is denoted by $w^+_{i,j+1/2}$

The vector of state quantities w can be discretized by volume averaging:

$$w_{k,i,j}=\frac{1}{\Delta_jR\Delta\phi}\int_{R_{j-\frac{1}{2}}}^{R_{j+\frac{1}{2}}}dR\int_{\phi_{i-\frac{1}{2}}}^{\phi_{i+\frac{1}{2}}}d\phi w_k(R,\phi),\qquad k=1,2,3. \tag{30}$$

In this way a piecewise constant representation of the state quantities is obtained. Equation (3) becomes, for every cell (i,j),

$$\Delta_jR\Delta\phi\frac{\partial}{\partial t}w_{i,j}=\Delta_jR\Delta\phi s_{i,j}(w,R,\phi)-\Delta\phi(f_{i,j+\frac{1}{2}}-f_{i,j-\frac{1}{2}})$$
$$-\Delta_jR(g_{i+\frac{1}{2},j}-g_{i-\frac{1}{2},j}). \tag{31}$$

The discrete source term $s_{i,j}(w,R,\phi)$ is approximated by $s(w_{i,j},R_j,\phi_i)$. The problem left is the evaluation of the fluxes $f_{i,j\pm\frac{1}{2}}$ and $g_{i\pm\frac{1}{2},j}$ at the cell interfaces. This is done by *upwind differencing*, which method will be briefly explained below. More detailed descriptions are given by, e.g., van Leer (1977, 1985), Harten et al. (1983), and Woodward and Collela (1984).

In upstream differencing the flux $f_{i,j+\frac{1}{2}}$ at the interface between cells (i,j) and $(i,j+1)$ is assumed to depend on the state quantities $w^+_{i,j+\frac{1}{2}}$ and $w^-_{i,j+\frac{1}{2}}$, where the superscripts denote the result of some kind of interpolation from the average value in a cell to the average value on the boundary of the cell (Fig. 1a). Because in general $w^+_{i,j+\frac{1}{2}}\neq w^-_{i,j+\frac{1}{2}}$, there is a discontinuity at the interface between the cells (i,j) and $(i,j+1)$ in our numerical representation. To avoid ambiguities, we will reserve the term *interface* for continuous functions: the interface $(i,j+\frac{1}{2})$ is the line segment separating cell (i,j) and $(i,j+1)$. The flux across this interface is denoted by $f_{i,j+\frac{1}{2}}$. For a function that is discontinuous at the interface, we define its value at the *boundary* of cell (i,j) near the interface $(i,j+\frac{1}{2})$ as the average over the line segment between $\phi_{i-\frac{1}{2}}$ and $\phi_{i+\frac{1}{2}}$ in the limit for $R\uparrow R_{j+\frac{1}{2}}$. For the state quantity w we thus have

$$w^+_{i,j+\frac{1}{2}}=\lim_{R\uparrow R_{j+\frac{1}{2}}}\frac{1}{\Delta\phi}\int_{\phi_i-\frac{1}{2}\Delta\phi}^{\phi_i+\frac{1}{2}\Delta\phi}d\phi w(R,\phi). \tag{32}$$

The simplest type of interpolation from the cell averages to the boundary values is zeroth-order interpolation: $w^+_{i,j+\frac{1}{2}}=w_{i,j}$ (Fig. 1b). This yields a first-order-accurate scheme. Higher-order extensions can be made by a more complex type of interpolation. Let us leave this subject for a moment and just assume that $w^+_{i,j+\frac{1}{2}}$ and $w^-_{i,j+\frac{1}{2}}$ are known. Then the computation of $f_{i,j+\frac{1}{2}}(w^+_{i,j+\frac{1}{2}},w^-_{i,j+\frac{1}{2}})$ basically is a one-dimensional problem. Con-

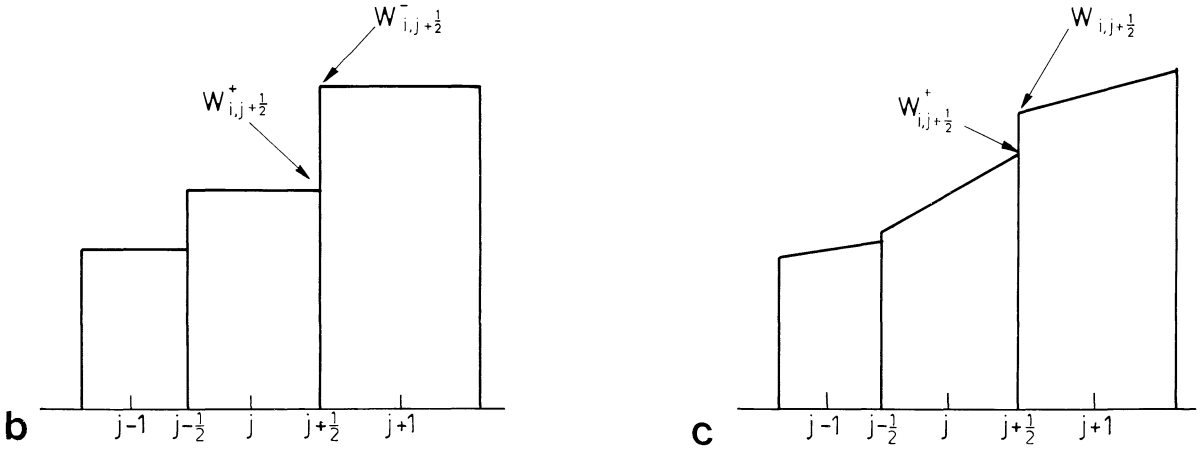

Fig. 1. b One-dimensional cross-cut at constant ϕ_i for a first-order scheme, showing one component of the vector of state quantities. The boundary values $w^+_{i,j+1/2}$, etc., are obtained by zeroth-order interpolation from the cell averages w_{ij}. **c** As **b**, but for a second-order-accurate scheme. The boundary values are obtained by first-order interpolation. The discrete state-quantities are assumed to be piecewise linear

sistency requires $f(w,w)=f(w)$. In general $w^+_{i,j+\frac{1}{2}} \neq w^-_{i,j+\frac{1}{2}}$. In the case of zeroth-order extrapolation, the physical analogue is an infinite tube with gas in two states, separated by a diaphragm. As soon as the diaphragm opens, the gas starts streaming. The solution of this so-called Riemann problem is time-dependent, but yields a unique time-independent state at the position of the diaphragm. This unique value $w_R(w^+_{i,j+\frac{1}{2}}, w^-_{i,j+\frac{1}{2}})$ can be used to evaluate $f_{i,j+\frac{1}{2}}=f(w_R)$. In the case of supersonic flow, w_R equals the initial state quantities at the upwind or upstream side, hence the name of the method. The original scheme that solves the Riemann problem exactly at each interface is named after Godunov (1959). The numerical evaluation of w_R involves a transcendental equation, which makes the method less attractive for large-scale computations. Various approximate Riemann-solvers have been proposed that solve the Riemann problem within an error of the order of the discretization error (for instance: Roe, 1981; Osher et al., 1983). In this paper, *flux-splitting* will be used for the upwind differencing. Flux-splitting can be considered as an approximate Riemann-solver, although it does not recognize stationary contact-discontinuities. The method splits the flux in a forward and backward component:

$$f(w^+_{i,j+\frac{1}{2}}, w^-_{i,j+\frac{1}{2}}) = f^+(w^+_{i,j+\frac{1}{2}}) + f^-(w^-_{i,j+\frac{1}{2}}). \tag{33}$$

The Beam-scheme (Sanders and Prendergast, 1974) is basically a flux-splitting scheme. It was re-invented by Steger and Warming (1981). Here we use a continuously differentiable version due to van Leer (1982). It emerges as the best scheme in the comparative study by van Albada et al. (1982). For the present problem we have

$$\begin{aligned} f^+ &= f = R\varrho \begin{pmatrix} u \\ u^2+c^2 \\ uv \end{pmatrix} && \text{if} \quad u \geqq c, \\ f^+ &= \frac{R\varrho}{4c}(u+c)^2 \begin{pmatrix} 1 \\ 2c \\ v \end{pmatrix} && \text{if} \quad |u| < c, \\ f^+ &= 0 && \text{if} \quad u \leqq -c. \end{aligned} \tag{34}$$

For the flux in the ϕ-direction we have

$$\begin{aligned} g^+ &= g = \varrho \begin{pmatrix} v \\ uv \\ v^2+c^2 \end{pmatrix} && \text{if} \quad v \geqq c, \\ g^+ &= \frac{\varrho}{4c}(v+c)^2 \begin{pmatrix} 1 \\ u \\ 2c \end{pmatrix} && \text{if} \quad |v| < c, \\ g^+ &= 0 && \text{if} \quad v \leqq -c. \end{aligned} \tag{35}$$

The f^- and g^- follow likewise. Note that the exact upwind values are obtained in the supersonic case. In the subsonic case an approximate solution to the Riemann problem is obtained. The splitting in the non-isothermal case can be found in a paper by van Leer (1982).

We now return to the subject of the interpolation of the state quantities. From the cell averages $w_{i,j}$ we would like to find the line averages at the cell boundaries, for instance $w^+_{i,j+\frac{1}{2}}$. Zeroth-order interpolation simply sets $w^+_{i,j+\frac{1}{2}} = w_{i,j}$, resulting in a first-order-accurate discretization. In this way the discrete representation is piecewise constant. Discontinuities in the flow are placed at the interfaces between cells, giving rise to numerical errors of the order of the gridsize. These numerical errors must always contain a dissipative term in order to satisfy the entropy condition (Harten et al., 1983). This guarantees that the correct physical solution is obtained. On the other hand, the presence of numerical dissipation causes the details of the solution to be smeared out.

The accuracy of the discretization can be improved by a more sophisticated interpolation to determine the quantities of Eq. (32) on both sides of an interface (van Leer, 1977; Collela and Woodward, 1984). The interpolation does not have to be carried out on the conserved state quantities w. Any set of quantities $q(w)$ which has a one-to-one correspondence with w in principle can be used. An important restriction on the interpolation is that it should be *monotone*. It must not create under- or overshoots, since these create numerical oscillations in the solution. Consider for the moment a one-dimensional distribution q_j. Then the interpolated value $q^+_{k,j+\frac{1}{2}}$ of the k^{th} component at the right boundary of cell j must obey the relation $q_{kj} \leqq q^+_{k,j+\frac{1}{2}} \leqq q_{k,j+1}$ to ensure monotonicity.

In this paper we use a first-order interpolation, which yields a second-order-accurate discretization. A linear distribution is computed in every cell by monotone interpolation (Fig. 1c). The discontinuities at the interfaces still remain, but they are an order of magnitude smaller in smooth regions of the flow, thus reducing the discretization error. Because the dissipative term of the discretization error is reduced as well, the second-order-accurate solution will generally show more detail then a first-order one on the same grid.

The linear distribution of a quantity q in a cell can be described by the components of the gradients in the R- and ϕ-direction:

$$q(R,\phi) = q_{ij} + \frac{(\phi-\phi_i)}{\Delta\phi}(\overline{\Delta_\phi q})_{ij} + \frac{(R-R_j)}{\Delta_j R}(\overline{\Delta_R q})_{ij},$$

with

$$\frac{|\phi-\phi_i|}{\Delta\phi} < \frac{1}{2} \quad \text{and} \quad \frac{|R-R_j|}{\Delta_j R} < \frac{1}{2}. \tag{36}$$

The computation of the average differences $(\overline{\Delta_\phi q})_{ij}$ and $(\overline{\Delta_R q})_{ij}$ is basically a one-dimensional affair. In the ϕ-direction

$$(\overline{\phi_\phi q})_{ij} = \text{ave}(q_{i+1,j} - q_{ij}, q_{ij} - q_{i-1,j}). \tag{37}$$

The procedure $\text{ave}(\Delta_+, \Delta_-)$ should yield $\frac{1}{2}(\Delta_+ + \Delta_-)$ in smooth regions of the flow. A smaller value must be chosen in the presence of discontinuities to preserve monotonicity. A smooth limiting-averaging procedure has been given by van Albada et al. (1982):

$$\begin{aligned} \text{ave}(\Delta_+, \Delta_-) &= \frac{1}{2}(\Delta_+ + \Delta_-)\left\{1 - \frac{(\Delta_+ - \Delta_-)^2}{\Delta_+^2 + \Delta_-^2 + 2\varepsilon_\phi^2}\right\} \\ &= \frac{(\Delta_-^2 + \varepsilon_\phi^2)\Delta_+ + (\Delta_+^2 + \varepsilon_\phi^2)\Delta_-}{\Delta_+^2 + \Delta_-^2 + 2\varepsilon_\phi^2}. \end{aligned} \tag{38}$$

Here ε_ϕ is a small bias of the order $\Delta\phi$ for the ϕ-direction [*not* $(\Delta\phi)^{3/2}$ as stated by van Albada et al., 1982], preventing division by zero and clipping of smooth extrema. A proper value for ε_ϕ, and similarly for ε_R, can be determined during the numerical iteration process, as will be described in Appendix I and Sect. 3.5.

For the R-direction the same procedure is used, but now a correction is included to compensate for the fact the grid is non-equidistant:

$$(\overline{\Delta_R q})_{ij} = \text{ave}(h_j^+(q_{i,j+1} - q_{ij}), h_j^-(q_{ij} - q_{i,j-1})),$$

with

$$h_j^+ = \frac{2\Delta_j R}{\Delta_j R + \Delta_{j+1} R} \quad \text{and} \quad h_j^- = \frac{2\Delta_j R}{\Delta_j R + \Delta_{j-1} R}. \tag{39}$$

Once the $\overline{\Delta_R q}$ and $\overline{\Delta_\phi q}$ are computed, the values at the interface follow immediately, for instance,

$$q^+_{i,j+\frac{1}{2}} = q_{ij} + \tfrac{1}{2}(\overline{\Delta_R q}), \tag{40}$$

from which $w^+_{i,j+\frac{1}{2}}$ can be found.

So far, the quantities q have not been specified. Following van Leer (1977), the natural choice for q is the set of characteristic variables. One-dimensional experiments in Paper I favour these variables as well.

The determination of the state quantities at the cell interfaces involves the following steps. First, the state quantities are transformed to the characteristic variables. Then, the differences of the characteristic variables across cell interfaces are averaged by Eqs. (37) or (39). The average differences in the characteristic variables are transformed back to average differences in the state quantities. The latter are used to determine the state quantities at every cell boundary, from which, finally, the split fluxes are computed.

For the present problem this procedure is described in Appendix I. As an additional feature, the interpolation of the rotational velocity v is carried out differentially with respect to the axisymmetric rotational velocity $v_c = (\omega_0(R) - \omega)R$. The interpolation of v_c is done explicitly, outside the limiting-averaging procedure. In this way, the result is more accurate than if v_{ij} would be used for the interpolation, especially near the centre where v_c is rather steep. This approach has the attractive property that in the axisymmetric case the solution (13) is an *exact* solution of the numerical equations. The same is true for the first-order scheme, if such a scheme is constructed by setting the average differences $\overline{\Delta_R q}$ and $\overline{\Delta_\phi q}$ to zero.

It should be emphasized that the interpolation and the computation of fluxes are carried out separately. Interpolation is performed on quantities describing the *state* of the gas, and provides values at the boundaries of each cell. This is the mathematical stage of the numerical scheme. The values at the two sides of an interface are used to compute the flux across that interface, thus describing the *flow* of the gas. This part is the physical stage of the discretization. Mixing the two, by performing the interpolation and limiting on the fluxes, may severely degrade the accuracy of the solution, as shown in Paper I. Similar problems may arise in Flux-Corrected Transport methods (Boris and Book, 1973), as demonstrated by van Albada et al. (1982). In the latter, some interpolation is done before a timestep, whereas limiting and interpolation is performed after the timestep, which is equivalent to operating on the fluxes.

3.2. Discretization in time

In this paragraph we will discuss the discretization of the upwind-differenced Euler equations in time. The right-hand side of Eq. (31) can be written as $r^n_{ij} = r_{ij}(w^n)$ and is called the residual. The superscript denotes the situation at time t^n. For a timestep $\Delta^n t = t^{n+1} - t^n$ we let

$$\frac{\Delta_j R \Delta\phi}{\Delta^n t} \int_{t^n}^{t^{n+1}} dt \frac{\partial w_{ij}}{\partial t} = \frac{\Delta_j R \Delta\phi}{\Delta^n t}(w^{n+1}_{ij} - w^n_{ij})$$
$$= \alpha r^{n+1}_{ij} + (1-\alpha) r^n_{ij}, \tag{41}$$

implying that the evolution of w per timesteps is based on a weighted mean of the residuals at the old and new time-level. The scheme is called *explicit* if $\alpha = 0$ and *implicit* otherwise. For $\alpha = 1$ we obtain the "backward Euler" scheme. This scheme will be used throughout.

Equation (41) can be linearized:

$$L^n(w^{n+1} - w^n) = \left[\frac{\Delta_j R \Delta\phi}{\Delta^n t} - \left(\frac{\partial r}{\partial w}\right)^n\right](w^{n+1} - w^n) = r^n(w). \tag{42}$$

Here $\left(\frac{\partial r}{\partial w}\right)^n$ is the Jacobian of r^n with respect to the state quantities w^n. Equation (42) behaves like an explicit scheme for small Δt. For large Δt, Newton's method for finding a zero-value solution of r is obtained. This property can be exploited by choosing Δt small if the residuals are large and Δt large if the residuals are small. For an initial guess w^0 of the solution, the residual will be large, so the integration in time will be explicit and fairly time-accurate. As the steady state is approached, the residual becomes smaller and the scheme gradually switches to Newton's method. Quadratic convergence can in principle be attained (Paper I).

In practice, the timestep is computed from the normalized residuals

$$\sigma_{ij} = \frac{\Delta_j R \Delta\phi}{\Delta^n t_{ij}} = \frac{1}{\varepsilon} \max_{k=1,2,3}\left(\frac{|r^n_{kij}|}{|w^n_{kij}| + h^n_{kij}}\right). \tag{43}$$

The term h_{kij} prevents division by zero: we use $h_{1ij} = 0$ and $h_{2ij} = h_{3ij} = w_{1ij} c$. Equation (43) determines a *local* timestep $\Delta^n t_{ij}$ which ensures that the local variation of the solution $w^{n+1} - w^n$ is at most of the order ε. We choose $\varepsilon = 1$ throughout this paper. Equation (43) differs from the definitions of Δt in Papers I and II, where the maximum over the entire grid was adopted. The present approach is better suited for problems with large spatial variations in the state quantities. The definition of the timestep by Eq. (43) makes the numerical scheme unconditionally stable and enables fast convergence to the steady state. The switching from small to large timesteps ensures that the correct steady state is approached.

There is one crucial problem left: the inversion of the linear system (42). We attack this problem by a powerful method, namely multigrid relaxation. This will be the main theme of the following paragraph.

3.3. Multigrid relaxation

The multigrid technique attempts to find a solution of a large set of not necessarily linear equations by considering them at several grids, from the finest where the solution has to be found, to a coarsest. It requires an operator to find an approximate solution at every grid: a *relaxation* operator. Also two operators are required to convey information between different grids: a *prolongation* operator brings information from a coarse to a fine grid, and a *restriction* operator does the opposite. The motivation for this approach lies in the fact that most relaxation schemes can adequately compute the high-frequency content of the solution, but have problems with the low-frequencies, which cover a larger part of the computational domain. By restriction every long wave can become a short one on one of the coarser grids. There the relaxation operator can take care of it very efficiently.

An introduction to this subject can be found in Brandt (1981). In the ideal case, a multigrid method solves the problem in an amount of work proportional to N, where N is the total number of cells on the finest grid. Of course, the constant of proportionality should not be too large. For elliptic equations it can be proven that the amount of work indeed obeys this proportionality to N in the asymptotic limit for large N (Hackbusch, 1981). The development of a multigrid scheme for *hyperbolic* equations of the type studied here, has taken some time, but successful results have been obtained in the last years (Jameson, 1983; Mulder, 1985a, Paper III).

The multigrid method applied in this paper will now be discussed. To shorten the notation, Eq. (42) is rewritten in standard multigrid form:

$$Lu=(\sigma I-M)u=f, \tag{44a}$$

where I is the identity matrix and

$$\sigma_{ij}=\frac{\Delta_j R\Delta\phi}{\Delta^n t_{ij}}, \quad M=\left(\frac{\partial r}{\partial w}\right)^n \quad \text{and} \quad f=r^n. \tag{44b}$$

The solution u updates w^n according to $w^{n+1}=w^n+u$. The matrix L consists of 3×3 blocks. Every block correspond to a cell. The total number of blocks in N^2, with $N=N_R\times N_\phi$. Fortunately, most of the blocks in this enormous matrix contain only zeroes. Consider for instance our first-order scheme. Then, according to Eqs. (31), (33), and (A 6) with the average differences set to zero, the residual is computed on a 5-point stencil:

$$r_{ij}^n=r(w_{i,j-1}^n, w_{i-1,j}^n, w_{i,j}^n, w_{i+1,j}^n w_{i,j+1}^n). \tag{45}$$

The matrix L consequently has one main-diagonal and 4 off-diagonals (in terms of 3×3 blocks). The rest is nought, leaving $5N$ blocks.

The residual for the discretization with second-order accuracy is computed on a 9-point stencil. To save storage and to avoid an increase in complexity of the code, we adopt an approximate linearization that has the same structure as the linearization of the first-order-accurate scheme and still preserves the homogeneity of the equations (see Appendix II). In this way, the same relaxation scheme can be used for the first-order- and second-order-accurate residual. The price paid for this simplification is some loss of convergence speed because Newton's method is only approximately obtained for large timesteps.

A relaxation scheme provides an approximate solution of (44) by inversion of a matrix $\tilde{L}$ that is a reasonable approximation to L. A comparison of various relaxation schemes for the upwind-differenced Euler equations can be found in Paper II. Here we use *symmetric line/Gauss-Seidel* (SLGS) relaxation. The line-part is performed in the periodic ϕ-direction. For a given ring j, an exact inversion is carried out on a matrix consisting of the main-diagonal blocks and the two off-diagonals corresponding to the ϕ- or i-direction. The diagonals corresponding to $j-1$ and $j+1$ are neglected. This leaves a cyclic block-tridiagonal system that can be solved by a standard procedure (see Appendix III). The solution on line j thus obtained can be subtracted from the right-hand side of (44a), for which the matrix M is used. Then the next line at $j+1$ is processed, which has already been influenced by the previous line-relaxation through the update with M. This technique is known as Gauss-Seidel relaxation. The symmetric component of the scheme comes in by first performing all line-sweeps with increasing j, from $j=1$ to N_R, and then repeating the line-inversions in the reverse direction, from $j=N_R$ to 1. Such a scheme has a good high-frequency damping (Paper II).

The complete SLGS relaxation scheme can be written as

$$\begin{aligned} s^{(m)} &:= \tilde{L}^{-1} f^{(m)}, \\ u^{(m+1)} &:= u^{(m)} + s^{(m)}, \\ f^{(m+1)} &:= f^{(m)} + M s^{(m)}. \end{aligned} \tag{46}$$

The initial values are: $f^{(0)}=f=r^n$ and $u^{(0)}=0$. The scheme can be repeated several times, as indicated by the superscripts m and $m+1$. The final solution $u^{(m_l)}$ is used to update w^n, according to $w^{n+1}=w^n+u^{(m_l)}$, after which the new residuals and the new linearization can be computed. Here we use $m_l=1$ for a single-grid SLGS relaxation step.

The accuracy of the single-grid, approximate solution $u^{(m)}$ can be improved by a multigrid *correction scheme* (CS). For the upwind-differenced Euler equations such a scheme has been described in Paper III. The CS tries to find a solution of the equation

$$Le=f^{(m)} \tag{47}$$

by using coarser grids. Here e is called the *defect*. The communication between fine and coarse grids is regulated by restriction and prolongation operators. Consider for instance a fine $N_\phi\times N_R$ grid and a coarse $(\frac{1}{2}N_\phi)\times(\frac{1}{2}N_R)$ grid. Restriction lets

$$f_{I,J}^{(0)}=f_{i,j}^{(m)}+f_{i+1,j}^{(m)}+f_{i,j+1}^{(m)}+f_{i+1,j+1}^{(m)}, \tag{48}$$

where $i=1,3,\ldots,N_\phi-1$ and $j=1,3,\ldots,N_R-1$ are indices on the fine grid and $I=\frac{1}{2}(i+1)$ and $J=\frac{1}{2}(j+1)$ on the coarse. Alternatively, the fine grid will also be denoted by the subscript f, the coarse by the subscript c. Writing the restriction operator as I_f^c abbreviates (48) to $f_c^{(0)}=I_f^c f_f^{(m)}$. Note that this restriction operator preserves the conservation form (3) on coarser grids. The linear system L_c can be found by addition of the corresponding blocks of M, whereas

$$\sigma_{I,J}=\max_{\substack{i,i+1\\ j,j+1}}(\sigma_{ij}) \tag{49}$$

controls the relative change of the solution. If the original residual is of the form (45), the coarse matrix L_c has the same structure as L_f and the same SLGS relaxation scheme can be used on the coarse grid:

$$\begin{aligned} s_c^{(m)} &:= \tilde{L}_c^{-1} f_c^{(m)}, \\ e_c^{(m+1)} &:= e_c^{(m)} + s_c^{(m)}, \\ f_c^{(m+1)} &:= f_c^{(m)} + M_c s_c^{(m)}, \end{aligned} \tag{50}$$

where the initial values are: $e_c^{(0)}=0$, $f_c^{(0)}=I_f^c f_f^{(m_l)}$.

The coarse grid correction $e_c^{(m_l)}$ is prolongated to the fine grid by the prolongation operator I_c^f. Here we take a trivial operator which simply distributes the coarse-grid values to the fine grid:

$$\begin{aligned} s_f^{(m)} &:= I_c^f e_c^{(m_l)} = e_c^{(m_l)}, \\ u_f^{(m+1)} &:= u_f^{(m)} + s_f^{(m)}, \\ f_f^{(m+1)} &:= f_f^{(m)} + M s_f^{(m)}. \end{aligned} \tag{51}$$

This introduces some interpolation errors on the fine grid which are effectively removed by an extra SLGS relaxation step.

Extension of the CS to more than two grids is straightforward. We use a coarsest grid of 2×2 cells and perform an exact inversion on that grid instead of the SLGS relaxation. On all the other grids, one SLGS step is made before restriction to a coarser grid, and one after each prolongation to a finer grid. This sequence is known as a *V-cycle*. The total number of relaxation steps per grid is 2, except on the 2×2 grid.

3.4. Boundaries

The final quasi-steady solution of the numerical equations will depend on the source term and the boundary conditions. The initial values are unimportant for the final solution. For fast convergence, however, the initial values should be fairly close to the quasi-steady state. Here we will concentrate on the boundary conditions.

In Sect. 3.1 a computational domain S has been defined by $R_{\min} \leqq R \leqq R_{\max}$ and $0 \leqq \phi \leqq \pi$. As the problem is periodic in 2ϕ, the boundaries in the ϕ- or i-direction are treated in the same way as the interior cell boundaries. For the R- or j-direction the analytical solution at $R_{\min}$ and $R_{\max}$ is used. Assume that the bar ends at a certain cut-off radius R_{co}. Then the ϕ-dependence of the potential can be neglected for $R_{\max} \gg R_{co}$. We thus can use the axisymmetric solution at the outer boundary:

$$\varrho(R_{\max}) = \varrho_0\,, \quad v(R_{\max}) = v_c(R_{\max}) \quad \text{and} \quad u(R_{\max}) = 0\,. \tag{52}$$

At the centre things are less easy. Our potential has one Inner Lindblad Resonance (see Paper IV) and at a radius $R_{\min} \ll R_{ILR}$ the solution will contain no shocks. If, in addition, the cut-off radius $R_{co} \gg R_{ILR}$, then the potential around $R_{\min}$ is approximately

$$V(R,\phi) = R^{p+2}\{c_0 + c_2(0)\cos(2\phi)\}\,, \tag{53}$$

where c_0 and $c_2(0)$ are constants. If a small parameter $\varepsilon = c_2(0)/f_0$ with $f_0 = \{(p+2)c_0\}^{1/2}$ is introduced, a stationary solution up to order ε can be found:

$$\ln\varrho = \ln\varrho_c + \varepsilon R^{\frac{1}{2}p} A_0(R)\cos(2\phi)\,, \tag{54a}$$

$$u = \varepsilon R^{1+\frac{1}{2}p} A_1(R)\sin(2\phi)\,, \tag{54b}$$

$$v = \varepsilon R^{1+\frac{1}{2}p} A_2(R)\cos(2\phi)\,. \tag{54c}$$

Substitution of (54) in Eq. (8) yields, up to order ε:

$$(\omega_0 - \omega)A_0 = (1+\tfrac{1}{4}p)A_1 + \tfrac{1}{2}R\frac{dA_1}{dR} - A_2\,, \tag{55a}$$

$$(\omega_0 - \omega)A_1 - \omega_0 A_2 = -(1+\tfrac{1}{2}p)\omega_0 - \tfrac{1}{2}c^2/R^2\left(\tfrac{1}{2}pA_0 + R\frac{dA_0}{dR}\right), \tag{55b}$$

$$\tfrac{1}{4}\omega_1^2/\omega_0 A_1 - (\omega_0 - \omega)A_2 = \omega_0 + c^2/R^2 A_0\,. \tag{55c}$$

Because c is small as compared to the unit of velocity, the terms of order $c^2 A_0$ may be neglected. A_1 and A_2 can then be solved from (55b) and (55c) and A_0 follows from (55a):

$$A_0 = p\omega_0/h_0\{(\omega_0 - 2\omega)/h_2 + 8\omega h_0[(1+\tfrac{1}{2}p)h_0 + \omega_0]/h_2^2\}\,, \tag{56a}$$

$$A_1 = (\omega_0/h_0)[A_2 - (1+\tfrac{1}{2}p)]\,, \tag{56b}$$

$$A_2 = [(1+\tfrac{1}{2}p)^2\omega + 4\omega_0 h_0]/h_2\,, \tag{56c}$$

where $h_0 = (\omega_0 - \omega)$ and $h_2 = \omega_1^2 - 4(\omega_0 - \omega)^2$. In the expression for A_0 we have used the fact that $\omega_0 = f_0 R^{\frac{1}{2}p}$, hence $\omega_1 = (p+4)^{1/2}\omega_0$ and $R\dfrac{d\omega_1}{dR} = \tfrac{1}{2}p\omega_1$. The denominators become zero if $h_0 = 0$, which happens at co-rotation, or if $h_2 = 0$, which occurs at the ILR or OLR. The solutions (54) and (56) can be used for the boundary conditions at $R_{\min}$, as long as $R_{\min}$ lies well within the ILR.

There is one parameter left: the average central density ϱ_c. This value can either be specified in advance and kept fixed, or it may be taken equal to the average in the ring $j = 1$ next to $R_{\min}$.

At the boundaries, flux-splitting is used in the same way as in the interior region of the computational domain. For the second-order scheme, however, some restrictions are necessary for the determination of the gradient in the cells next to the boundary. First, the weights in Eq. (39) that correct for the non-equidistant R-grid, have to be $h_1^- = h_{N_R}^+ = 2$ for the differences between boundary and the average values in the cell. Secondly, a distinction should be made between outgoing and incoming characteristics. The eigenvalues corresponding to q^R in Eq. (A 1a) are $\lambda_1 = u + c$, $\lambda_2 = u$, and $\lambda_3 = u - c$ for the first, second and third component of q^R, respectively. For a cell with $j = 1$, a characteristic variable q_k^R is outgoing if its corresponding eigenvalue $\lambda_k < 0$, and for $j = N_R$ if $\lambda_k > 0$. The numerical boundary conditions are stable if the outgoing signal is not contaminated with information from the outside. Therefore, *extrapolation* is used for outgoing characteristics, for instance, at $j = 1$:

$$q_{ki1} - q_{ki\frac{1}{2}} = \frac{(R_1 - R_{\min})}{(R_2 - R_1)}(q_{ki2} - q_{ki1}) = \frac{\frac{1}{2}\Delta_1 R}{(R_2 - R_1)}(q_{ki2} - q_{ki1}) \quad \text{if} \quad \lambda_k < 0\,. \tag{57}$$

For incoming characteristics the difference with respect to the prescribed boundary values is adopted. The resulting differences are used as input for Eq. (39).

The extrapolation described by Eq. (57) is based on the underlying assumption that the flow is smooth near the boundary. In choosing the grid, care should be taken that there are always a few rings near the boundaries of the computational domain that contain no discontinuities. Of course, one can always set the extrapolated differences to zero for safety.

3.5. *Program control*

In this paragraph some practical aspects of the code are described. These are: (i) some quantities for the description of the performance of the method, (ii) the stopping criteria, (iii) acceleration of the program by freezing of the linearization, and (iv) successive grid-refinement.

The state of convergence can be measured by a norm of the residual:

$$\mathrm{RES}^n = \max_{i,j}(\mathrm{RES}_{ij}^n)/\mathrm{RES}^0\,, \tag{58}$$

where $\mathrm{RES}^0 = \max_{i,j}(\mathrm{RES}_{ij}^0)$ as computed from the axisymmetric initial values. A quasi-steady solution is obtained when RES^n vanishes. For a single-grid relaxation scheme we may plot *convergence histories* of RES^n vs. the number steps. In order to make a fair comparison with the multigrid scheme, a quantity "work" is introduced. It is defined as the number of times that the SLGS relaxation step is applied, normalized to the number of points on the finest grid. Thus, a single-grid relaxation step requires an amount of work 1, and a multigrid V-cycle $2(1+\frac{1}{4}+\frac{1}{16}+\ldots) \simeq 2\frac{2}{3}$.

A quantitative measure for the convergence speed is defined by

$$\tau = -\frac{\Delta\,\text{work}}{\Delta\log_{10}(\mathrm{RES})}, \tag{59}$$

being the amount of work required to reduce the residual by a factor 10.

The iteration process has converged to the quasi-steady state when the deviation from this steady state is much smaller than the discretization error. For solutions of Type I (Sect. 2.5), where there is net average inflow per ring $\langle w_2\rangle$, the constancy of the inflow over the computational domain can be used as a stopping criterion. Instead of $\langle w_2\rangle$, the numerical scheme will tend to make the following quantities constant:

$$a_{j+\frac{1}{2}} = \langle f_1^+(w_{i,j+\frac{1}{2}}^+) + f_1^-(w_{i,j+\frac{1}{2}}^-)\rangle\,, \tag{60}$$

being the average mass-flux across the interface between rings j and $j+1$. The average is taken by summation over $i = 1, \ldots, N_\phi$, and normalization by N_ϕ. The discretization error generally causes $a_{j+\frac{1}{2}} \neq \langle w_2\rangle_j \neq \langle w_2\rangle_{j+1}$ for all j. We choose to stop the

iterations if $a_{j+\frac{1}{2}}$ is constant within 1% over all rings $j=0, 1, \ldots, N_R$. The deviation of $\langle w_2 \rangle_j$ from this average inflow gives an indication of the discretization error. For solutions of Type II with $\alpha_M \neq 0$ [see Eq. (24)], the above does not hold any more. In that case we stop the iteration process if $\mathrm{RES}^n \leqq 10^{-4}$. This value functions as machine-zero for our FORTRAN single-precision (about 6 significant digits) computations.

The amount of cpu-time required to obtain a converged solution may be shortened by freezing the linearization L^n as given by Eq. (42). Instead of computing L^n at every iteration n, the matrix is kept constant during a number of iterations. The matrices required for the block-tridiagonal line-inversions can be stored in memory as well (see Appendix III), and also the restricted linearizations on the coarser grids of the multigrid scheme. One thus avoids the computation of a new linearization, part of the line-inversions, and the restriction for a number of steps, which leads to substantial savings of cpu-time. To control the freezing a number of levels is defined, namely 0.3, 0.1, 0.03, 0.01 etc. As soon as RES^n drops below the first level, the matrices are frozen, until the next level is reached. There anything is recomputed and frozen again, until the next lower level is reached, etc. In the case that RES^n rises from below to above a certain level, the freezing is postponed for a number of steps.

The computation of ε_R and ε_ϕ (Sect. 3.1, Appendix I) may be controlled in the same way. As soon as a new level is reached, these constants can be determined by Eq. (A 7). Then a new linearization is computed, and the iteration process continues as described above. The new values ε_R and ε_ϕ usually introduce some high-frequency components which result in a sudden increase of RES^n, but these are effectively removed in the next step.

Instead of the axisymmetric initial conditions, a solution on a coarser grid (not to be confused with the coarser grids of the multigrid correction scheme) can be used. For instance, first a solution on a 8×8 grid can be computed to a residual, say, $\mathrm{RES}^n \leqq 10^{-2}$. This solution is interpolated to a 16×16 grid to serve as an initial guess, etc. On the finest grid, on which the actual solution is desired, the computation is carried out until the inflow per ring is constant within 1% (for Type I solutions), or until $\mathrm{RES}^n \leqq 10^{-4}$ (for Type II solutions). This technique is known as *nesting* or *successive grid-refinement*. To allow a fair comparison between runs with or without successive grid-refinement, we always use the RES^0 as computed from the axisymmetric initial values, even if nesting is used.

During the initial phase of the iteration process, the residuals are still large. The state quantities still vary considerably from step to step. The linearization is not very constant either. This implies that the linear system (42) is already solved with sufficient accuracy by a single-grid relaxation step. The multigrid correction scheme does more work than is required. Therefore, we use single-grid relaxation as long as $\mathrm{RES}^n > 0.1$, and proceed with the multigrid correction scheme once RES^n has dropped below this level.

Finally, we remark that the velocities are scaled to the sound speed c in the numerical computations. The potential is rescaled correspondingly. The initial uniform density $\varrho_0 = 1$.

4. Results

4.1. Model parameters

As a standard problem we use a potential with a power $p = -1.8$ and axial ratio of the bar $b/a = 0.8$. The bar is cut off at a radius R_{co} by means of a weighting function. For R_{co} we choose either CR or the OLR. The constants of Eq. (6) become: $c_0 = 2.2858$ and $c_2(0) = -0.019587$ at the centre. The function $c_2(R)$ maintains its central value along the larger part of the bar, until, near R_{co}, the weighting function causes its decrease. Outside R_{co}, where the material bar ends, we have $c_2(R) = -4.6052\,10^{-3}\,(R/R_{\mathrm{co}})^{-3.2}$. The quantity $q_t(R)$, as defined by Sanders and Tubbs (1980), equals $-2c_2(R)/((p+2)c_0)$. In the present example $q_{t,\max} = q_t(0) = 8.6\%$. The sound speed is chosen to be 0.035.

For practical purposes, the unit of length is chosen as 1 kpc, the unit of velocity as $250\,\mathrm{km\,s^{-1}}$, and the unit of surface density as $3\,M_\odot/\mathrm{pc}^2$. The sound speed hereby becomes $8.75\,\mathrm{km\,s^{-1}}$.

The resonances in the plane of the galaxy are described by the ratio $(\omega_0 - \omega) : \omega_1$, where ω_0 is the rotational frequency as given in Eq. (13), ω_1 the epicycle frequency as given in Eq. (16), and ω the pattern speed of the bar. For $\omega = 0.1$, the Inner Lindblad Resonance [ILR, $(\omega_0 - \omega) : \omega_1 = 1 : 2$] occurs at a radius 1.86, the Inner Ultra-Harmonic Resonance (IUHR, 1 : 4) at 5.00, co-rotation (CR, $\omega_0 = \omega$) at 8.36, the Outer UHR ($-1 : 4$) at 11.87, and the Outer Lindblad Resonance (OLR, $-1 : 2$) at 15.49 model units of length.

These parameters yield a Type I solution (Sect. 2.5) if the bar ends at CR. This type of solution has a net average inflow and no shocks outside CR. Due to this inflow, the central density will continue to rise. A quasi-steady solution is forced by setting $\varrho_c = \varrho_0 = 1$.

A Type II solution is obtained if the material bar is cut off at the OLR. An additional source term (24) is used with $\alpha_M = 3.5\,10^{-4}$. The corresponding timescale $\tau_M = 11$ Gyr.

4.2. Convergence speed

In this paragraph the performance of the method is considered. The reader who is not interested in numerical techniques may continue with Sect. 4.3.

The performance of the integration scheme and the accuracy of the spatial discretization is investigated by comparing the numerical results for four Type I solutions. These are computed with identical parameters but on two different grids, namely with 32×32 and 64×64 zones, and with first-order and second-order spatial accuracy.

The best results in terms of convergence speeds are expected for a first-order scheme, since the linearization (42) is exact in that case. Figure 2 shows convergence histories for a 32×32 and a 64×64 grid. The multigrid scheme is clearly superior in performance during the later stages of convergence.

The iteration process can be split in two parts: an *evolution* or *searching* phase and a *relaxation* or *convergent* phase. During the first, the solution varies considerably, in the second the slope of the convergence history is almost constant. In the latter phase, Newton's method is fully applicable and the multigrid correction scheme performs best. It is precisely this relaxation phase where most explicit schemes lose their convergence speed, or even may not convergence at all, due to their incapability to dampen the low-frequency components of the residual.

The iterations for the Type I solution are stopped as soon as the average inflow per ring is constant within 1%. Figure 2 shows that the multigrid scheme reaches this point at a higher level of RES^n than the single-grid scheme. This is due to the superior damping of all frequencies by the multigrid scheme. The residual norm RES^n of Eq. (58) tends to favour the high-frequency components of the residual. Thus, for a given value of RES^n, the multigrid scheme provides a more accurate solution than the single-grid scheme, in which the low-frequency component of the residual is still large.

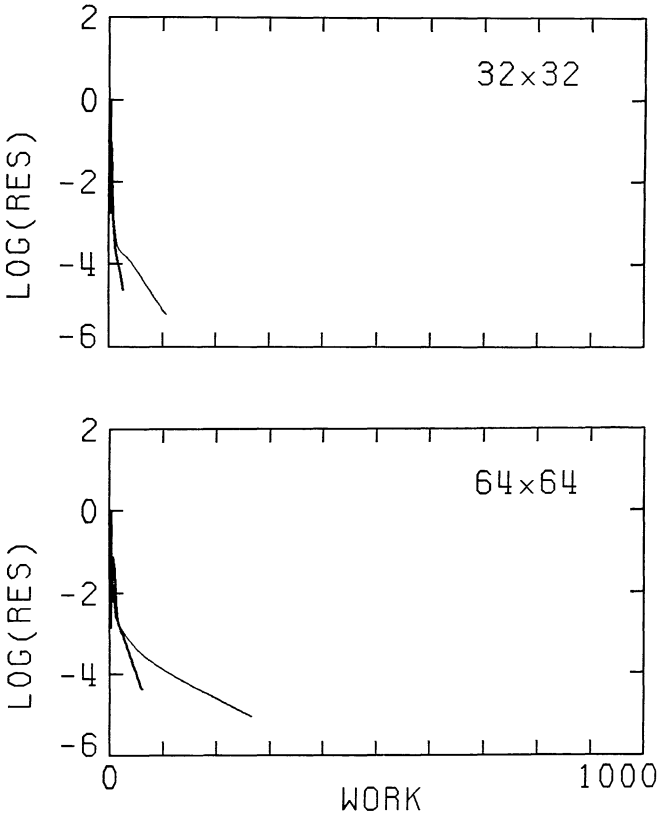

Fig. 2. Convergence histories for the first-order-accurate solutions on a 32×32 and a 64×64 grid. In both cases the multigrid scheme (thick line) is more efficient than the single-grid scheme (thin line)

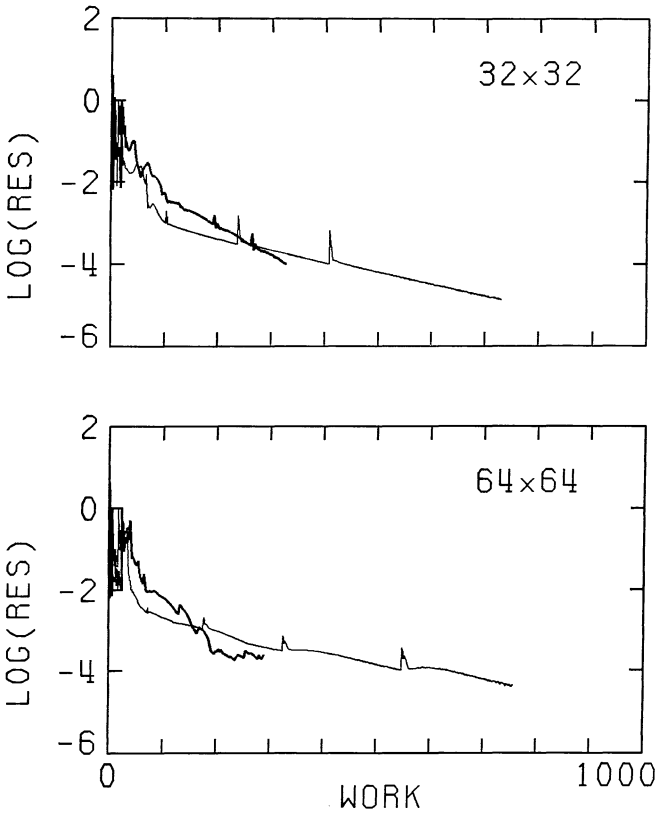

Fig. 3. Convergence histories for the second-order-accurate solutions on a 32×32 and a 64×64 grid. Again the multigrid scheme (thick line) is faster than the single-grid scheme (thin line)

Figure 3 shows the convergence histories for the second-order-accurate solutions. Again the multigrid scheme is more efficient than the single-grid scheme. The glitches in the relaxation phase of the iteration process are caused by the recomputation of ε_R and ε_ϕ (Sects. 3.1, 3.5, and Appendix I). At the end of the 64×64 run the effect of numerical round-off errors becomes visible. The same is true for the single-grid run, but here the effect is less pronounced. Because the multigrid scheme combines data from the entire grid, starting from the 64×64 up to the coarsest 2×2 grid, it is more sensitive to round-off errors than the single-grid scheme. A 128×128 grid would definitely require double-precision arithmetic (about 14 significant digits per number).

Convergence for the second-order runs is considerably slower than for the first-order-accurate solutions. One expects the incomplete linearization to result in a loss of convergence speed, both for the single-grid and multigrid scheme. The effect on the latter may be worse, since the multigrid scheme tries to improve the approximate result of the single-grid scheme, which already might be more accurate than justified by the incompleteness of the linearization. The faster convergence of the multigrid runs shows that this is not yet case, at least not in the convergent phase.

However, the incomplete linearization is not the only cause of the observed slow-down. The second reason is the difference in structure of the various solutions. The first-order solutions have a fair amount of numerical dissipation that causes details to be smeared out. Consequently, it is much easier to reach a quasi-steady state. The second-order solutions contain a higher amount of detailed structure and our integration scheme has to work harder to find a solution. Figure 4 shows the density distributions of the various solutions. The main direction of the flow, measured in the non-rotating frame, is clockwise. The contrast has been enhanced by normalization with the average density per ring $\langle \varrho \rangle_j$. This causes the spiral arms to stand out clearly. The increase in detail when going from a first-order to a second-order spatial discretization is impressive. The second-order solution on the 32×32 grid is even slightly better than the 64×64 first-order result. Both require about the same amount of cpu-time, about 45 min on our VAX 11/750.

It should be remarked that Fig. 4 has been obtained from the cell averages by a monotone first-order interpolation. For the second-order-accurate solutions this a little crude. In principle, second-order interpolation with shock-fitting can be used for the latter, since all the information is available, but this has not been attempted.

Because of the variations between the solutions mentioned above, it is hard to make any definite statements about the behaviour of our integration scheme for a large number of cells N. An ideal method yields a number of iterations or "work" independent of N, in the limit for large N. In order to test this on a specific problem, one either needs a simple problem like that in Paper III, where the asymptotic behaviour already sets in for relatively small N, or one has to go to very fine grids for a more complicated problem like the one described here. We have refrained from doing so for two reasons. First, our second-order 64×64 solutions has sufficient accuracy for modelling purposes. A multigrid run takes nearly 3 h to converge, using 2.5 Mbytes of virtual memory. Secondly, a 128×128 computation would require 2×4 times as much memory (the factor 2 accounts for the

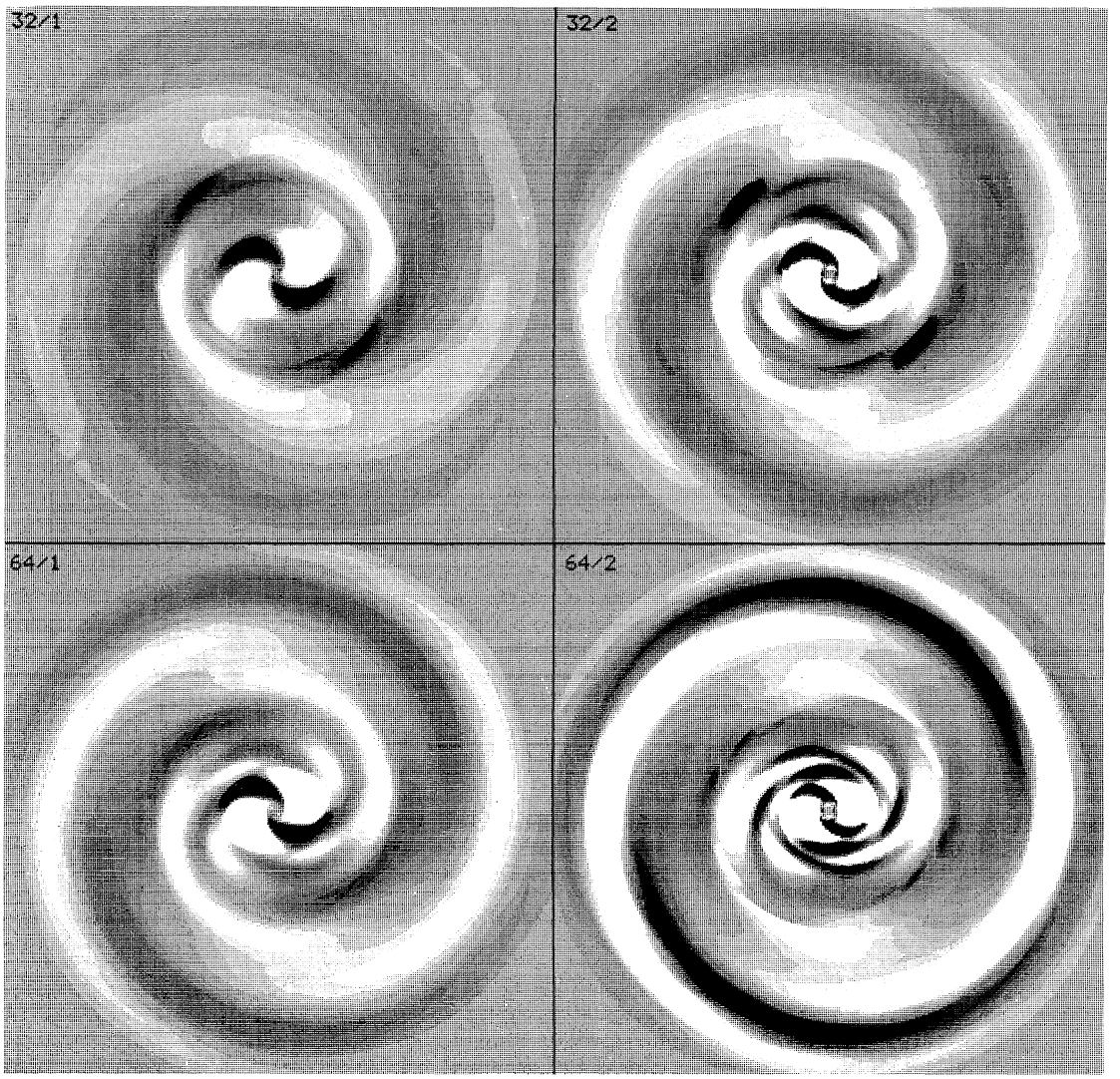

Fig. 4. The logarithm of the density scaled by the average density per ring, $\ln(\varrho/\langle\varrho\rangle)$. A darker shade corresponds to a higher density. The upper row shows the solutions on a 32×32 grid, the lower on a 64×64 grid. The results on the left are first-order- and on the right second-order-accurate. Each side of a figure corresponds to 40 units of length. The ILR is at 1.22, CR at 8.36 and the OLR at 15.49

double-precision arithmetic and storage, expected to be required for grids finer than 64×64), which is well above the 5 Mbytes virtual memory limit of our VAX 11/750.

The superiority of the multigrid scheme with respect to a single-grid scheme is obvious for the first-order runs. For the second-order runs, the difference between the two looks smaller. However, if one compares the slopes of the convergence histories for the 64×64 runs in Fig. 3, and neglects the noisy part just above 10^{-4} due the single-precision round-off errors, it is clear that the multigrid scheme has a much better damping than the single-grid scheme. The ratio of τ, as defined in Eq. (59), for the multigrid scheme and the single-grid scheme is about 0.19 during the convergent phase of the second-order 64×64 runs. The gain in efficiency with respect to a single-grid scheme is sufficient to justify the additional effort of coding the multigrid correction scheme. The actual improvement for an arbitrary problem will strongly depend on the required level of convergence and the structure of the flow.

4.3. Global properties of the quasi-steady solutions

In this paragraph the global structure of the quasi-steady solutions is described. We investigate the effect of the parameters required to obtain a steady state, namely, the fixed central density ϱ_c and the parameter α_M of Eq. (24). The timescales of the suppressed unsteady processes are estimated to check the validity of the quasi-steady solutions. The global transport properties are considered by plots of the ring-averages of the state quantities.

We start with the Type I solution, which has only shocks inside CR. Figure 5 shows the averages per ring of the quantities $\ln(\varrho)$, u/c, v/c, and w_2/c. The dissipation in the shocks causes the gas to be swept inward. This effect is visible in the density shown in Fig. 5. The density is low in the region of the shocks. The material swept inward, is dumped in a ring with high density at the end of the shocks, at a radius somewhat inside the ILR. The region with the shocks is replenished by gas from the reservoir outside CR.

The above solution was computed with a fixed average central density ϱ_c, as in the preceding paragraph. To study the dependence

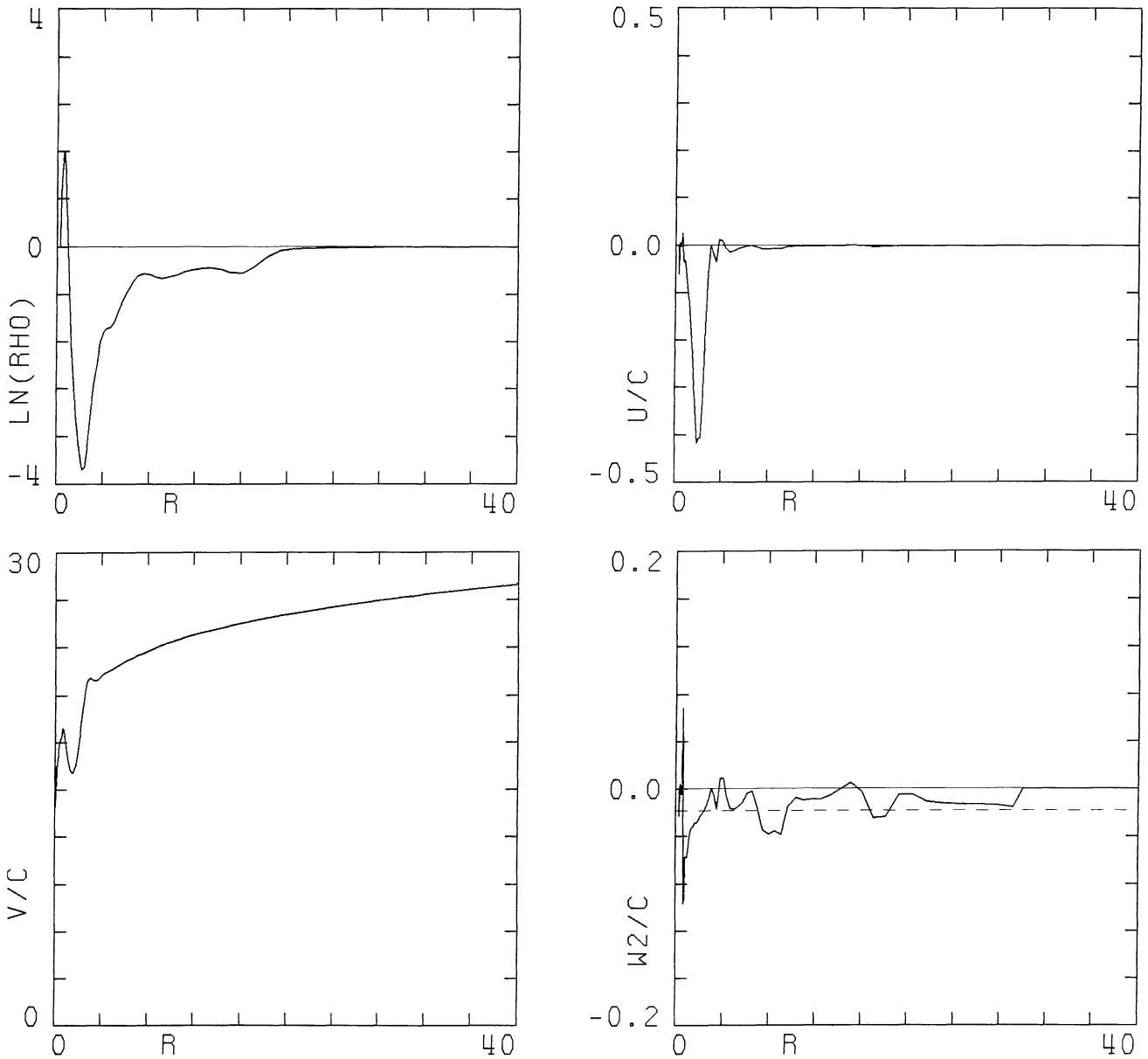

Fig. 5. Averages per ring for the 64 × 64 second-order Type I solution with a fixed average central density $\varrho_c = 1$. The dashed line in the plot of w_2/c indicates the average value of the $a_{j+1/2}$, that are constant within 1% for all j. The deviations from this line give an impression of the numerical discretization error

of the quasi-steady state on this central density, two additional runs were made: one with the average central density fixed at $\varrho_c = 10$, and one with varying ϱ_c equal to the average in the ring $j = 1$. In the latter, we find a final $\varrho_c = 3.05$ when the solution has become steady. Figure 6 shows the averages per ring of $\ln(\varrho)$ for these two runs. Apart from the very centre, there is hardly any difference between the various solutions. The differences are even smaller for the ring-averages of u/c, v/c, and w_2/c (not shown). Thus, the exact value of the average central density ϱ_c is not very important for the final flow pattern. It should be remarked, however, that the convergence for a run with varying ϱ_c is somewhat slower than in the case of a fixed value. The Euler equations of our problem are homogeneous of the degree 1 in the density. This implies that the density of a quasi-steady solution, when multiplied by an arbitrary factor, yields another quasi-steady solution. An unique result can only be obtained by the specification of a fixed boundary value. If ϱ_c is allowed to float freely, the density obtains its scale solely from the given value at the outer boundary. This causes the slower convergence.

The averages per ring, as shown in Fig. 5, provide some insight in the global transport properties of a Type I solution. Here we recall that the computational grid extends from a radius 0.3 to 30. Furthermore, as can be seen in Fig. 4, the spiral arms die out at a radius of about 20. Outside that radius the solution behaves almost, but not entirely, as an axisymmetric one. There, the value of the inflow $\langle w_2 \rangle$ is determined by the numerical viscosity μ_{num}. Because $\langle w_2 \rangle$ must be constant throughout the computational domain, the non-axisymmetric solution inside a radius of about 20 must adapt itself to this value, even in the presence of shocks. As mentioned in Sect. 3.5, the numerical computation is stopped if the average radial mass flux across the boundaries of ring j, i.e., $a_{j\pm\frac{1}{2}} = \langle f_1 \rangle_{j\pm\frac{1}{2}} = \langle R\varrho u \rangle_{j\pm\frac{1}{2}}$ is constant within 1%. In general, the value

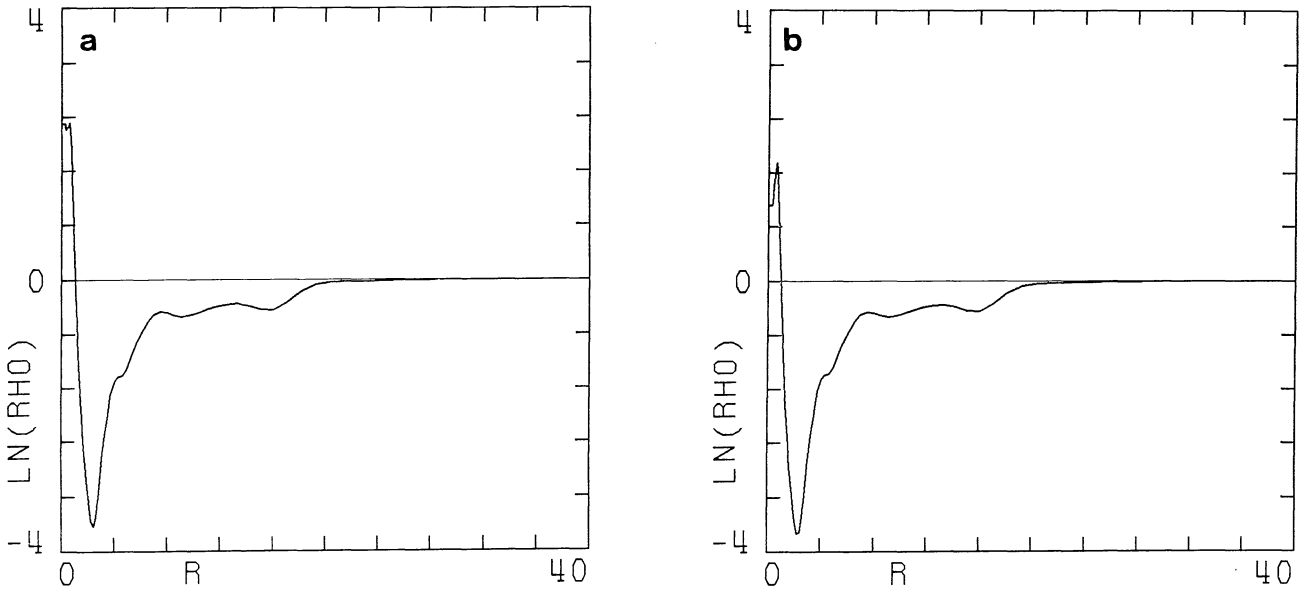

Fig. 6. a The average density per ring for a 64 × 64 second-order Type I solution with a fixed average central density $\varrho_c = 10$. **b** The same as **a**, but for a ϱ_c equal to the average in the ring $j=1$. The final value becomes $\varrho_c = 3.05$. Note that there is hardly any difference between the Figs. 5, 6a and b, apart from the centre

of $\langle w_2 \rangle_j = \langle R\varrho u \rangle_j$ inside the ring j will deviate from the average flux $a_{j\pm\frac{1}{2}}$ across the boundaries of that ring because of the numerical discretization error. The plot of $\langle w_2/c \rangle$ in Fig. 5 shows that these deviations are of the same order as the constant $a_{j\pm\frac{1}{2}}$ itself. This can be expected, as the constant inflow is determined by the same discretization error at larger radii.

One may wonder what happens to the quasi-steady solutions if one goes to increasingly finer grids. The numerical discretization error will become smaller, and so will the inflow rate. The shocks, however, will still drive the gas towards the centre, so $\langle u \rangle$ will maintain its size in the region of shocks. As a result, the average surface density $\langle \varrho \rangle$ in this region must become smaller on finer grids. Consequently, the *exact* quasi-steady solution of the inviscid Euler equations does not make sense. On very fine grids, viscosity must be added explicitly, i.e., the full Navier-Stokes equations should be solved, to obtain a physically relevant solution.

To assess the reliability of the present solutions, we have to examine the sensitivity of the state quantities to the numerical viscosity μ_{num}. The expression for Bernoulli's constant H, Eq. (9), reveals that the velocities u and v are strongly coupled to the potential $V(R, \phi)$. The surface density comes in as $c^2 \ln \varrho$, where the sound speed c is small. Thus a large change in the surface density will barely influence the velocities. In reverse, small deviations in the velocities will be strongly reflected in the density. As a consequence, the velocities u and v of the quasi-steady solution are quite well determined, but the surface density is not. A comparison between the four solutions of Fig. 4 shows that $\varrho/\langle \varrho \rangle$, u, and v can be computed quite accurately. The average surface density per ring $\langle \varrho \rangle$ is only qualitatively correct.

The average mass outflow for a Type I solution $\dot{M} = 2\pi a_{j\pm\frac{1}{2}}$, where $a_{j+\frac{1}{2}}$ is constant for all j. For the 64×64 second-order-accurate solution we obtain a value $\dot{M} = -4.13\,10^{-3}$. This result is obtained both for $\varrho_c = 1$ and $\varrho_c = 10$ (within a few percent) and also for the varying ϱ_c that becomes 3.05. For the units given in Sect. 4.1, this corresponds to $-3.16\,10^{-3}\,M_\odot\,\text{yr}^{-1}$.

The small size of the inflow rate $\dot{M}$ and the sensitivity of the radial density distribution $\langle \varrho \rangle$ to the numerical viscosity that results from the discretization error, imply that in real galaxy they are both likely to depend on the large-scale effects of processes as shear, bulk and turbulent viscosity, star formation, mass loss by stars, supernovae, infall of intergalactic matter, etc., that are not considered in the present computations. The velocities u and v will be less sensitive to these effects.

The timescale for a significant change in angular momentum of the bar can be computed from $\tilde{L}_{\text{bar}} = 1.098$ and $\dot{L}_{\text{gas}} = -0.022$. For a unit of surface density $\varrho_0 = 3\,M_\odot/\text{pc}^2$ this results in a timescale for the *acceleration* of the bar $\tau_{\text{bar}} = 9\,10^2\,\text{Gyr}$. This value is comfortably large, in fact so large that it must be considerably affected by the numerical discretization error. The exchange of angular momentum between the bar and the gas is clearly not important.

We continue this paragraph with a Type II solution. The same parameters as above are used (see Sect. 4.1), but now the bar is cut off at the OLR and the extra source term (24) is included to avoid the depletion of the region around CR. The average central density is determined from the average in ring $j=1$.

The convergence history is given in Fig. 7. The speed of convergence is comparable to that of the preceding problem. The average central density becomes $\varrho_c = 12.4$ when the steady state is reached.

The averages per ring are shown in Fig. 8. The plot of $\langle \ln(\varrho) \rangle$ displays two rings. The shocks inside CR sweep the gas inward, as discussed in Sect. 2.5. The gas piles up in a ring where the shock ends, at a radius well within the ILR. Outside CR the gas is swept outward and a similar ring is created. The two rings are expected to be roughly of the gaussian form (16), apart from a modification due to the additional source term (24). The pumping of the shocks and the corresponding directions – inward inside and outward outside CR – are confirmed by the plot of $\langle u/c \rangle$ (Fig. 8): there is a change of sign at $R_{\text{CR}} = 8.36$. The inflow or outflow stops near the end of the shocks.

The source term (24) was introduced as a function describing the creation and annihilation of gas. From a numerical point of view it can be considered as a device to keep the density contrast

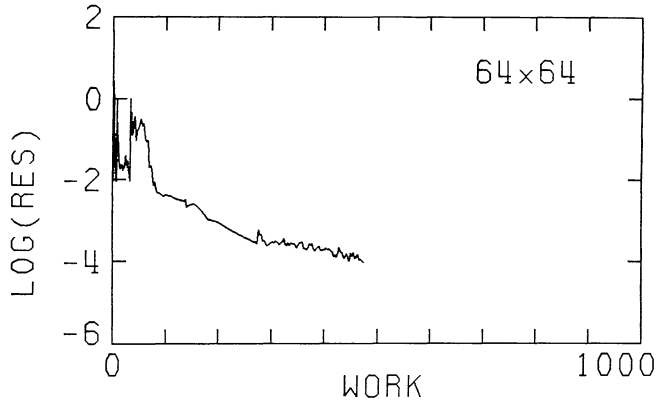

Fig. 7. The convergence history of a 64 × 64 second-order Type II solution, with varying central ϱ_c

within an acceptable range. The span of this range is determined by the value of α_M. A smaller value of α_M allows for a larger density contrast, with a higher density in the rings and a lower around CR. The present, rather arbitrary value avoids a contrast larger than can be handled by our single-precision code.

To study the dependence of the Type II solution on α_M, we made a run with $\alpha_M = 3.5\,10^{-5}$, i.e., 10 times smaller than the previous value. It turned out that the spiral pattern was hardly affected. The velocities u and v, and also $\varrho/\langle\varrho\rangle$, were practically the same as in the previous run. On the other hand, $\langle\varrho\rangle$ dropped by a factor of about 3 in the region of shocks; the size of $\langle w_2\rangle$ decreased by roughly the same factor, while maintaining the form of the original distribution as plotted in Fig. 8. For increasingly smaller α_M one expects the velocities u and v, and the normalized surface density $\varrho/\langle\varrho\rangle$ to remain practically the same, whereas $\langle\varrho\rangle$ and $\langle w_2\rangle$ will become increasingly smaller.

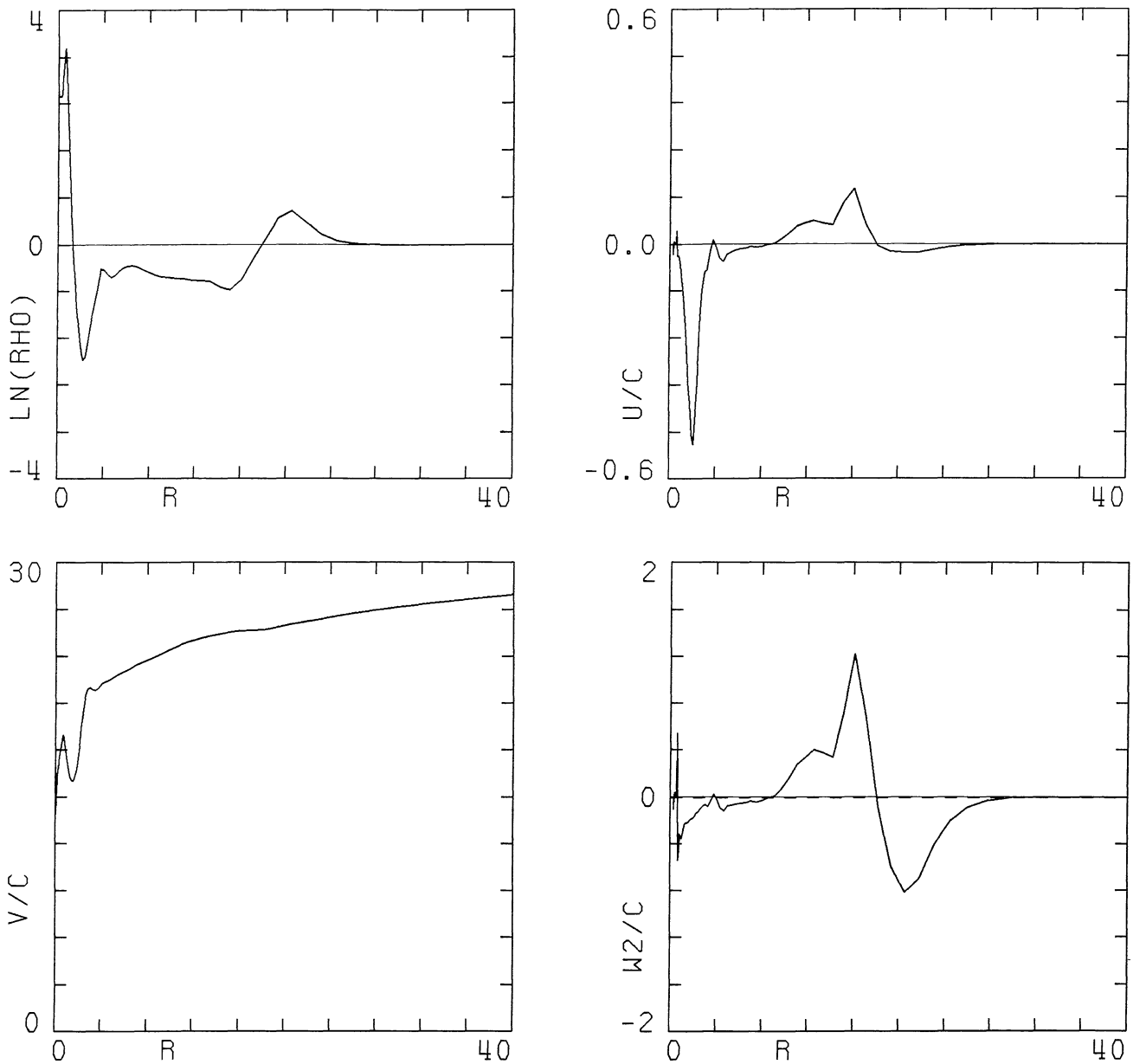

Fig. 8. Averages per ring for the 64 × 64 second-order Type II solution. The average central density finally becomes $\varrho_c = 12.4$

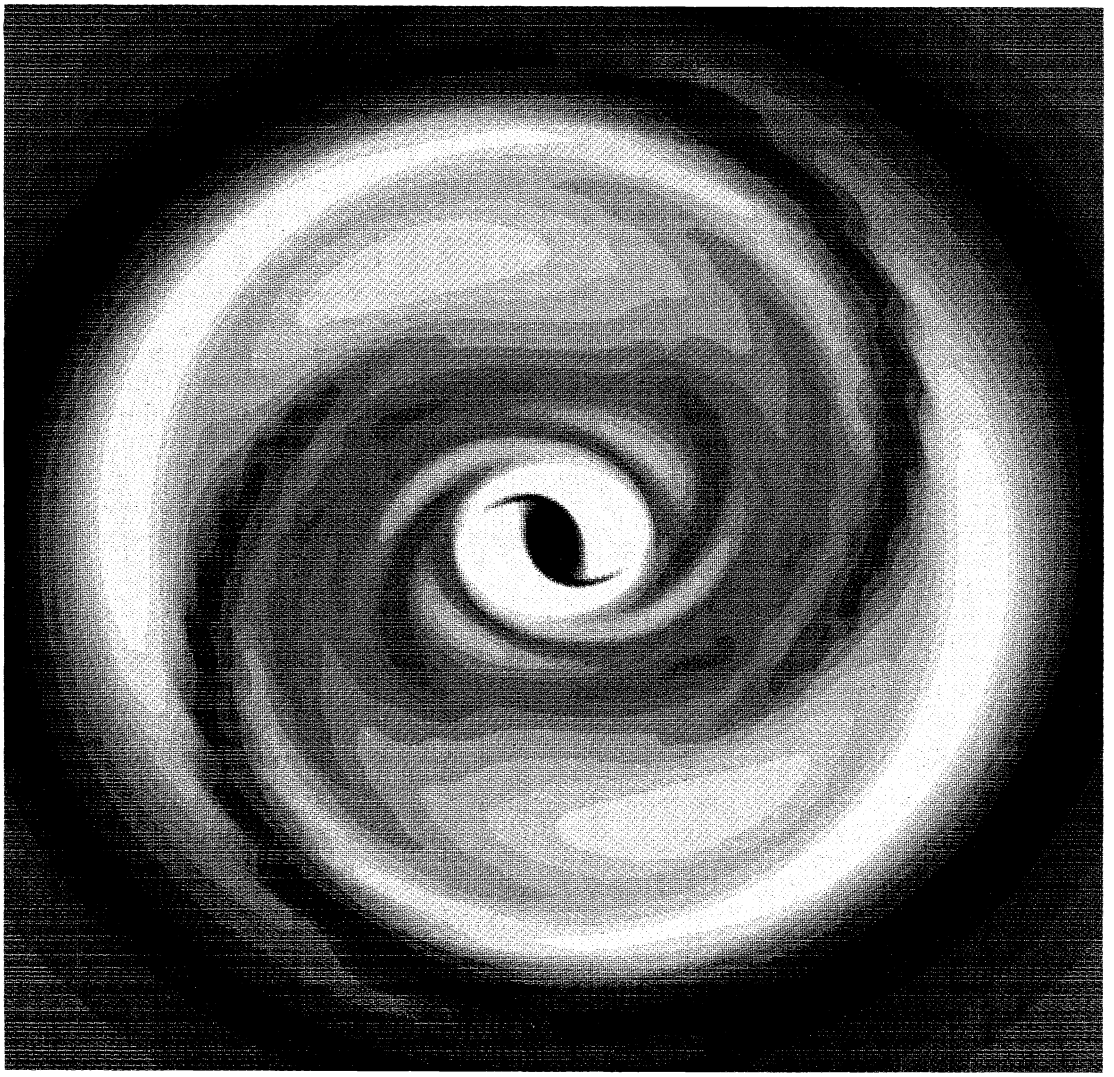

Fig. 9a. The logarithm of the two-dimensional surface density, $\ln(\varrho)$, for the 64 × 64 second-order Type II solution. A darker shade corresponds to a higher density. The length of a side is 40 units of length. CR is at 8.36. The polar grid is stretched in the R-direction, with a larger cell size for increasing R. This, in combination with the crude interpolation, causes the jagged irregularities near the shocks at larger radii. The flow is predominantly clockwise in the non-rotating frame

We thus find the same behaviour as for the Type I solution: the velocity field and the tangential distribution of the surface density, $\varrho/\langle\varrho\rangle$, are quite well determined, whereas the radial distribution $\langle\varrho\rangle$ and the systematic outflow $\langle w_2\rangle$ are strongly affected by α_M. This confirms the earlier conclusion that $\langle\varrho\rangle$ and $\langle w_2\rangle$ in a real galaxy are likely to be determined by other processes in addition to those considered here.

4.4. Spiral structure

Figure 9a shows the two-dimensional density distribution of the quasi-steady Type II solution, this time without the contrast enhancement of Fig. 4. The spiral arms and the locations of the main resonances are sketched in Fig. 9b. The two spiral arms within CR can be traced starting from the central ring. They are driven by the 1 : 2 resonance (ILR). A little more outward they are joined by two additional arms, driven by the 1 : 4 resonance (IUHR) and containing shocks as well. Near CR they all disappear. Outside CR we first pass the −1 : 4 resonance (OUHR), again driving two extra arms, and then the −1 : 2 resonance (OLHR), which generates strong shocks. The shocks die out eventually and the outer ring comes up.

The velocity field is presented in Figs. 9c and 9d. The first shows the radial velocity u/c, the second the tangential velocity with circular rotation subtracted, i.e., $(v-v_C)/c$ as given in Eq. (A 4). The velocity field has an elliptical character. Inside the ILR and outside the OLR the flow pattern, as viewed in the non-rotating frame, can be roughly described by ellipses with their long axis in the y-direction. Between the ILR and OLR the long axis coincides with the x-axis. A rotation of the streamline-ellipses over 90° occurs at the ILR and OLR. This behaviour has been described by Contopoulos (1980) while considering the shape of periodic orbits in a rotating barred galaxy.

The elliptical character of the flow pattern, with the associated rotation of ellipses at the Lindblad Resonances, casts doubt on the use of the *tilted-ring model*. This model has been introduced for the analysis of the velocity field in disk galaxies, as determined from neutral-hydrogen observations (cf. Rogstad et al., 1974; Bosma,

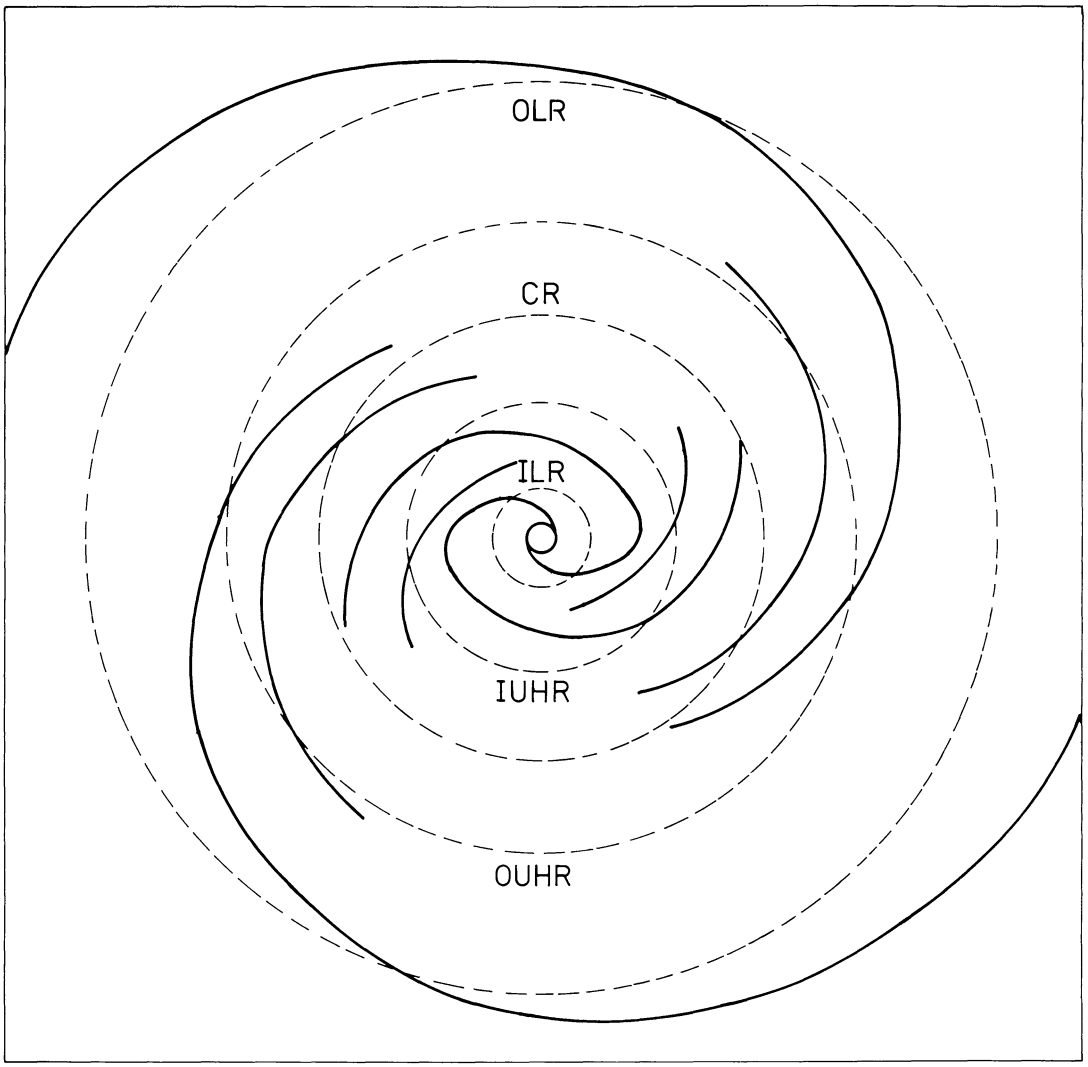

Fig. 9b. Sketch of the spiral arms in **a**. The main resonances are indicated by dashed lines

1981a, b). A set of ellipses is fitted to the observed velocity field and then interpreted as a set of *circles* each with a specific inclination and position angle of its line of nodes. In this way, the circles often appear to lie in different planes, so the galaxy must be warped. The present results, however, show that a *rotated-ellipse model*, with the ellipses in the same plane, is an equally feasible interpretation of the observed velocity field.

A Type II solution is generated if the gravitational potential of the bar outside CR is strong enough to shock the gas. Here we obtained such a result by letting a weak bar extend up to the OLR. If one prefers to cut off the bar at CR, which is more realistic in view of observations (Kormendy, 1982), N-body simulations (Miller and Smith, 1979; Sellwood, 1981) and orbit calculations (Contopoulos, 1980), a Type II solution can still be obtained by a stronger bar. Alternatively, or in addition, the gravitational potential of the spiral arms, which has been neglected here, may provide the extra forcing required for shocks (Contopoulos, 1980). Finally, lowering the sound speed enables a weak bar to generate shocks outside CR, even if the bar ends at CR.

The main observable characteristics of the quasi-steady solution inside CR are the same for a Type I and a Type II solution. There is a central ring, from which two spiral arms emanate. At the IUHR a transition from two arms to four arms occurs. The shocks stand on the *inside* of the arms – an arm being defined by its higher density. Outside CR, the arms of the Type I solution have no shocks, whereas those of the Type II solution have shocks on the *outside*. In addition, the Type II solution has a distinct outer ring at the end of the spiral arms. The shocks are observable through their association with dust-lanes and by the velocity field of the galaxy. The relative strength of the ring is time-dependent (van Albada, 1985) and depends strongly on the viscosity and temperature of the gas, and on the properties of additional source terms of the type (24) that describe star formation, supernovae, etc.

A detailed comparison between the observable characteristics of our numerical solutions and real galaxies falls beyond the scope of this paper. However, a few remarks are appropriate. The transition from a two-armed to a four-armed spiral pattern identifies the location of the IUHR in a galaxy. This characteristic signature can be used to determine the pattern speed and the locations of the other resonances. A galaxy where this pattern can be recognized, is NGC 6951 (see Sandage, 1961). The bar in this galaxy must be stronger than the one used in our computations, but the main pattern can be clearly seen: a small ring near the centre, two almost straight dust-lanes going outward, and a

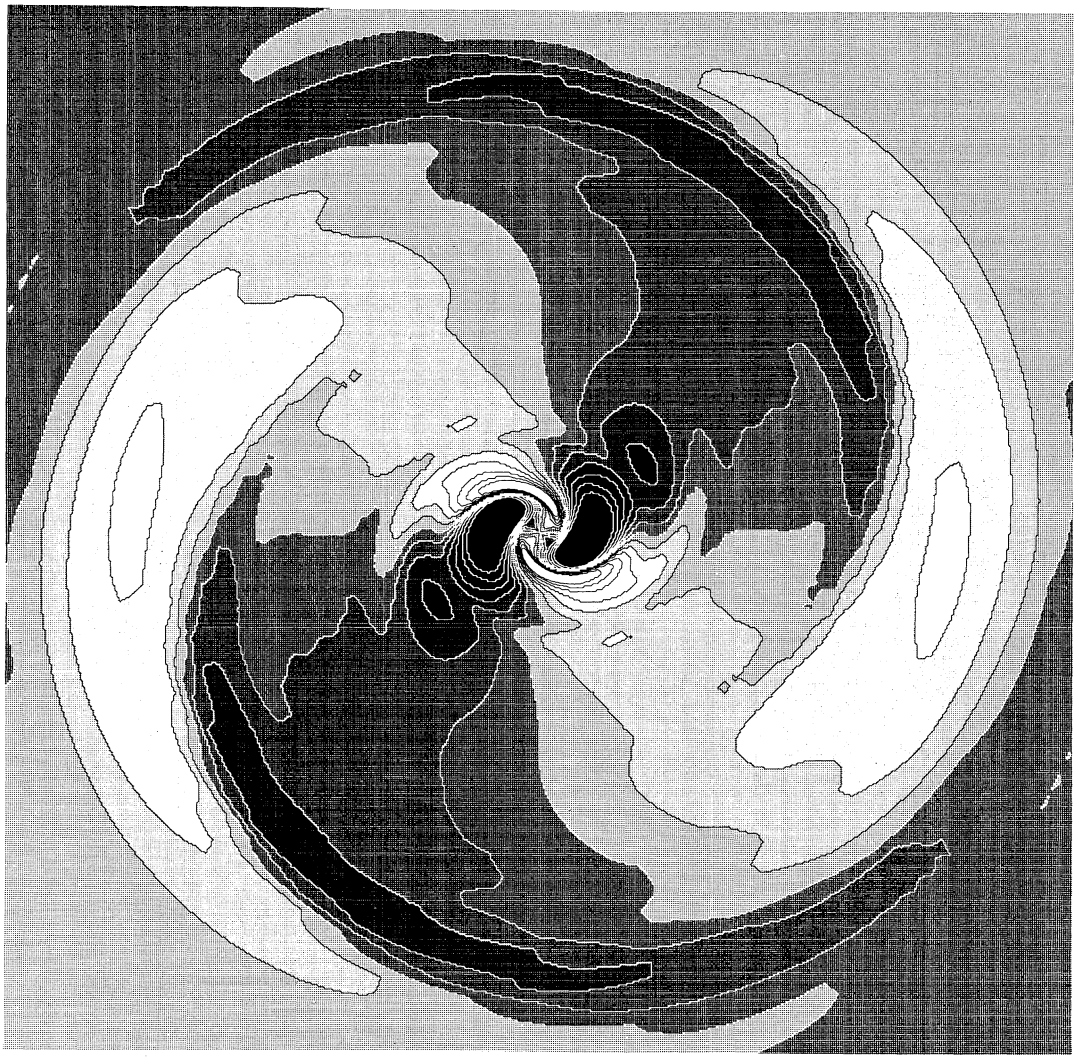

Fig. 9c. The radial velocity scaled to the sound speed, u/c, corresponding with **a**. Contours are drawn at integer values of the mach number u/c between -6 and 6. The lighter shades correspond to negative velocities, the darker to the positive

transition to four arms where the dust-lanes end. The visible bar ends where the two inner arms turn, at a radius somewhat inside the IUHR (cf. Fig. 9b). Nearly all optical structure visible in the Hubble Atlas (Sandage, 1961), is confined to the region within CR. In general, the neutral-hydrogen extent will be larger.

In comparing optical observations with the present solutions, one should keep in mind that our computations are restricted to simplified model equations for the total of *gaseous* components in a disk galaxy. Our computer program is suited for the efficient computation of models for the spiral arms and the velocity field as observed in neutral hydrogen and in other material that belongs to or correlates well with the gaseous components. A model for the neutral-hydrogen distribution in our own Galaxy will be described in a subsequent paper.

4.5. Rotation curves

From the Type II solution of the preceding paragraph we construct rotation curves as seen by an observer in the plane of the galaxy. These may be compared to the rotation curves obtained from neutral-hydrogen observations of edge-on disk galaxies.

Figure 10a shows the rotation-curve as obtained from an axisymmetric potential. The disk is cut off at $R=20$ units of length. The next figures (10b) display the effect of the $\cos(2\phi)$-term: a weak bar or oval distortion with axial ratio $b/a=0.8$. The pattern changes with varying angle ϕ_{obs} of the observer with respect to the x-axis, the long axis of the bar. This angle is measured counterclockwise.

Most outstanding is the velocity peak of the central ring, which reaches a maximum at $\phi_{\text{obs}}=90°$. Here the velocity rises well above the almost flat rotation curve. These velocities are usually qualified as "anomalous" in the literature.

Outside the inner ring there is a clear "hole" in the density distribution. The first, lightest gray-level is chosen to start just above zero, and the corresponding gas will in general be hardly observable. This gap corresponds to the region of lowest density in Fig. 9. The rotation curves clearly show loops associated with the various arms. The arms at the ILR and OLR stand out clearly, those of the Ultra-Harmonic Resonances are weaker. The velocity u can be fairly large at the shocks. This causes the arms to pass the line $R=0$ at a definitely non-zero velocity.

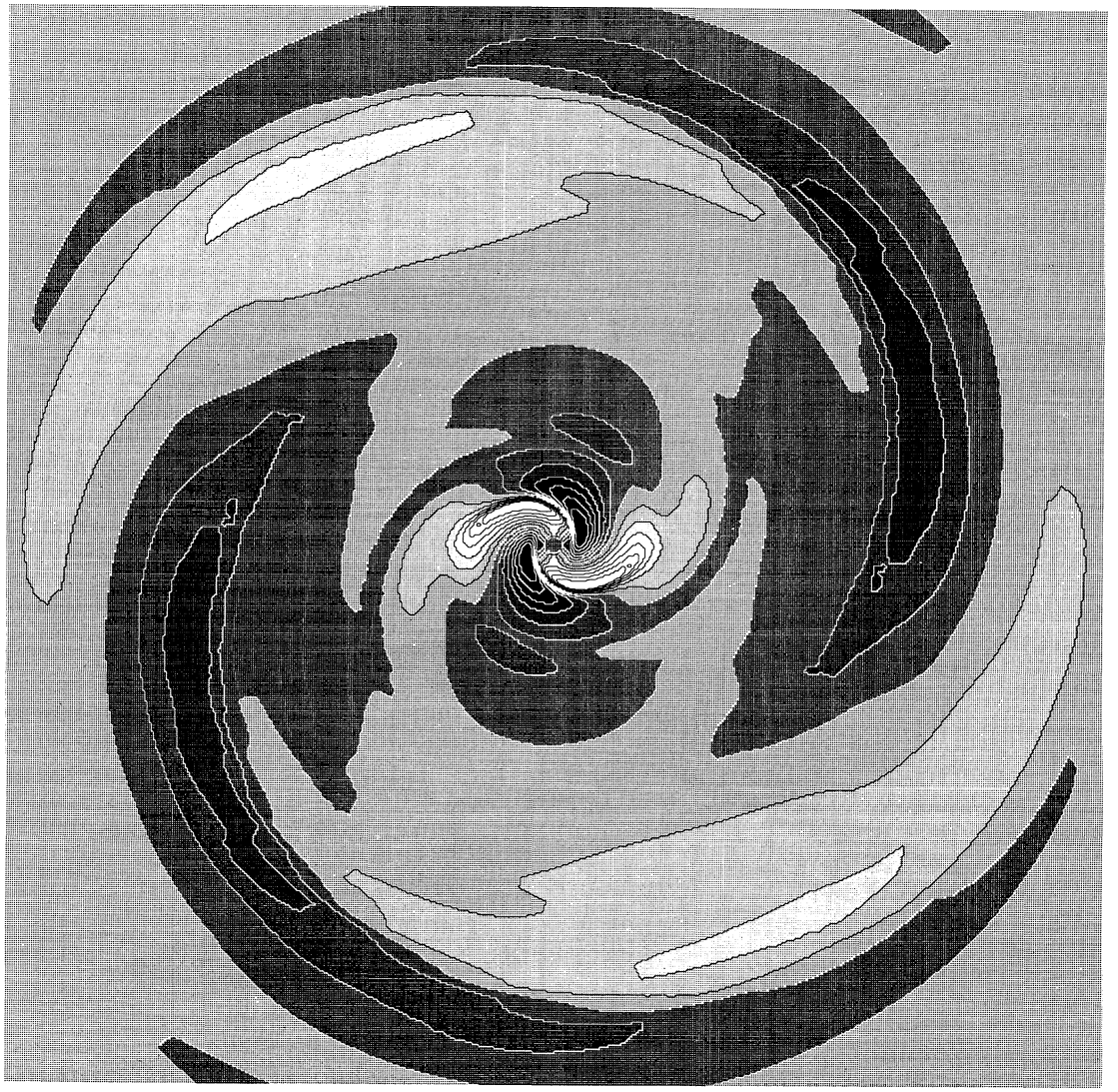

Fig. 9d. As **c**, but now for the tangential velocity with circular rotation substracted, i.e., $(v-v_c)/c$

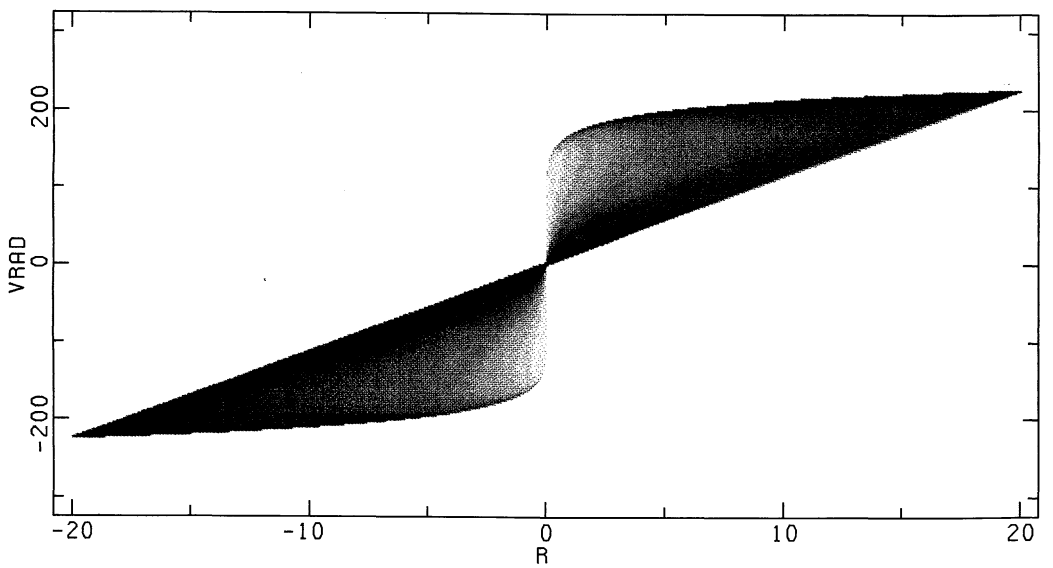

Fig. 10a. The rotation curve corresponding to the flow in the axisymmetric part of the potential. The density is constant in this case. Only the part within $R=20$ has been used for this figure

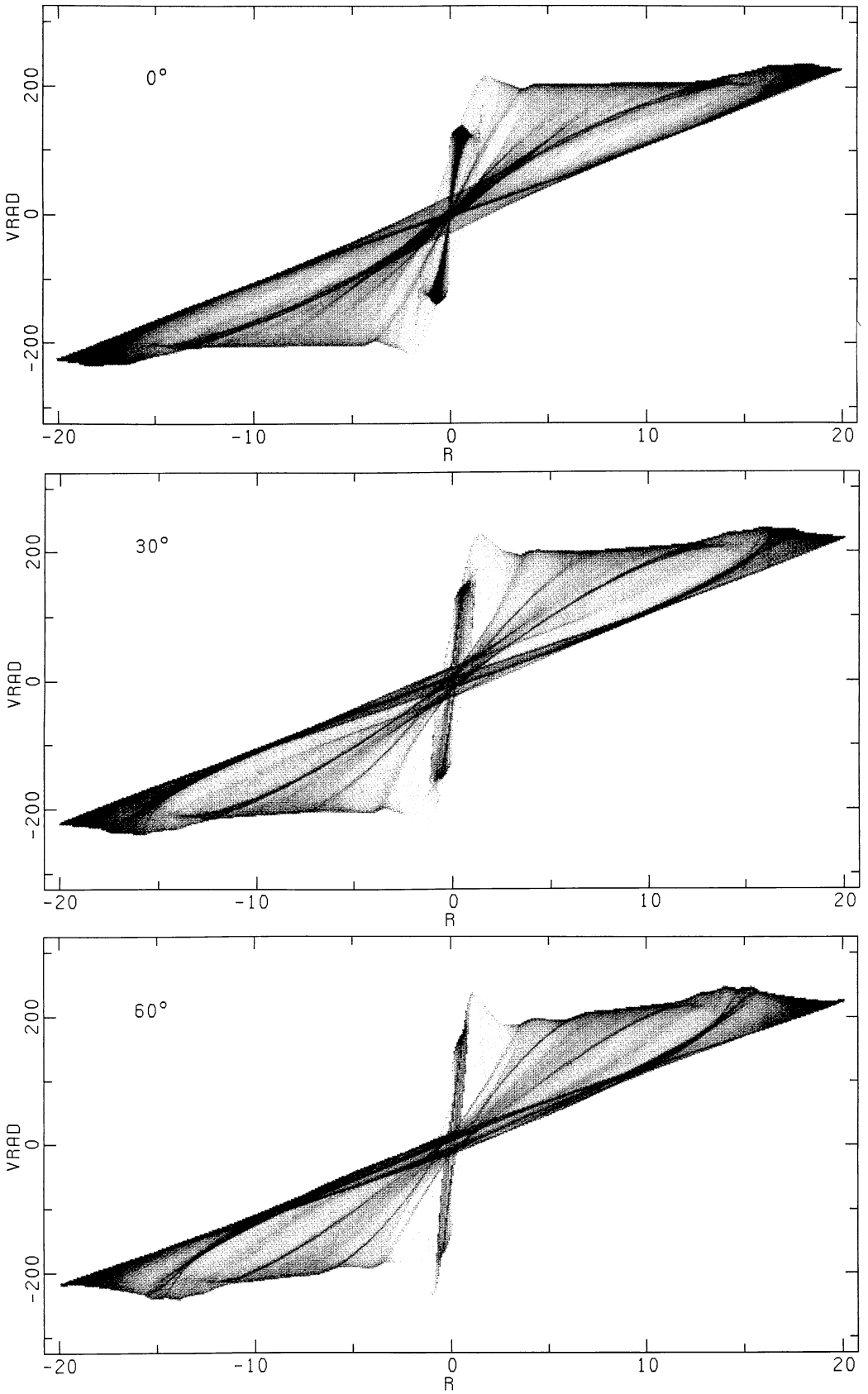

Fig. 10b. Rotation curves as seen by an observer in the plane of the galaxy. The curves are based on the 64 × 64 second-order Type II solution (cf. Figs. 7–9). The angle ϕ_{obs} is measured counterclockwise, starting from the direction of the long axis of the bar, which is the horizontal axis in Fig. 9. Approaching velocities are taken positive, contrary to the usual convention. The velocity scale is based on a unit of velocity $v_0 = 250\,\mathrm{km\,s^{-1}}$, the distance scale is in model units. Only the part of the solution within $R = 20$ has been used for these figures

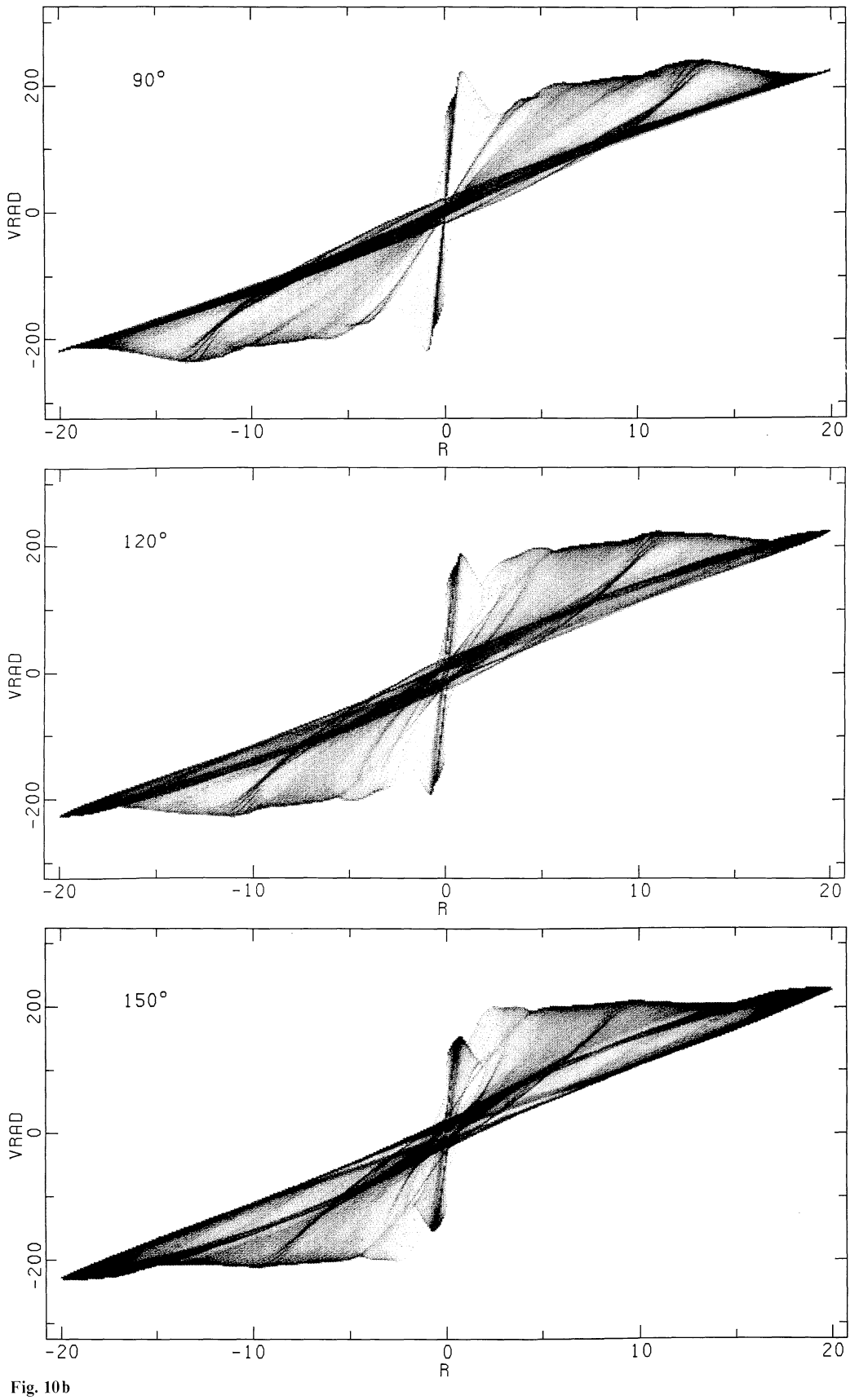

Fig. 10b

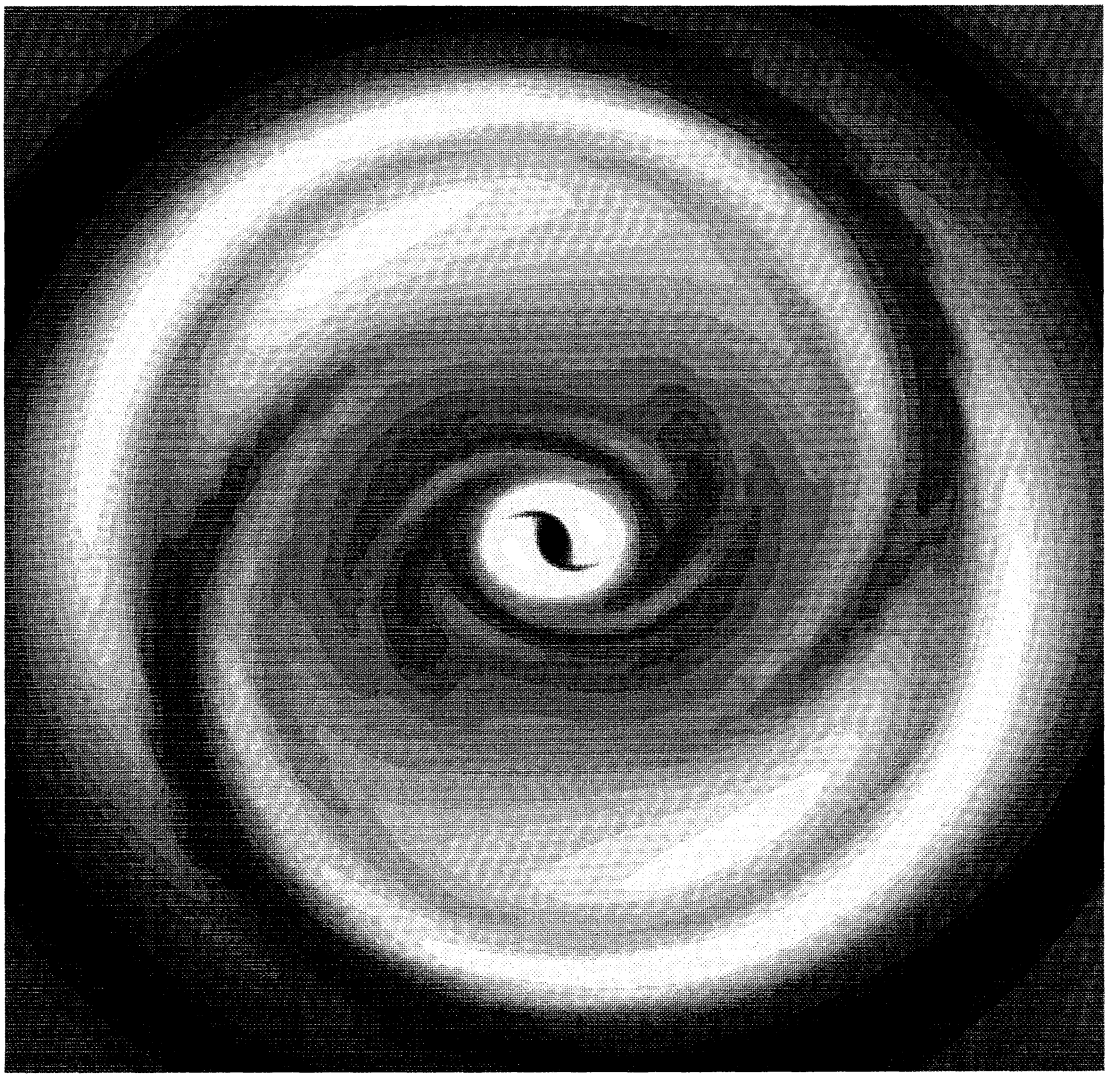

Fig. 11. As Fig. 9a, but for a potential with power $p = -1.6$ instead of -1.8. The pattern speed is chosen in such a way, that R_{CR} is the same for both figures, whereas the ILR now is at 1.30 and the OLR at 17.13

It must be emphasized that Fig. 10 is the result of a simple power-law potential, slightly deformed to contain a weak bar-like perturbation. The differences between Figs. 10a and 10b are due solely to this perturbation. An analysis of the rotation curves in terms of circular motions would obviously not reproduce the underlying mass-distribution of gravitating matter. The result would depend on the actual angle ϕ_{obs} of the observer. If an observed galaxy is not edge-on, nor face-on, a better impression of the underlying mass-distribution can be obtained on the basis of a rotation curve constructed by averaging per ring, with the correct deprojection. However, the plot of v/c in Fig. 5 shows that there still can be a significant deviation from a simple power law in that case. Therefore, one should not attempt to derive too refined mass-models from observed neutral-hydrogen rotation curves under the assumption of circular motion.

A property that is strongly associated with the underlying distribution of gravitating matter, is the spacing of the spiral arms. The power p of the power-law distribution determines the relative distances of the resonances. A change in p results in a different scaling in the R-direction. A larger value of p, for instance -1.6 instead of -1.8, causes the resonances, such as the ILR, IUHR, OUHR, and OLR, to lie farther away from CR. In this way, the region around CR is effectively enlarged, the pitch angle of the spiral arms increases, and the region near the centre shrinks. Figure 11 shows a Type II solution of this kind. The pattern speed ω has been given a larger value to yield the same R_{CR} as in the previous case.

5. Discussion and conclusions

5.1. Numerical method

The multigrid method described in this paper is an efficient tool for the computation of steady or quasi-steady solutions of the Euler equations. Its application to the problem of quasi-steady flow in a weakly barred galaxy provides accurate solutions in typically 500 work units. The method is recommended for computing steady discontinuous solutions of hyperbolic equations in general. These equations occur not only in astrophysics, but also in other disciplines, particularly in aerodynamics as an approximation to the Navier-Stokes equations.

The use of upwind differencing allows for the construction of a stable and efficient relaxation scheme, which is the most important ingredient of our multigrid method. Here we have used symmetric line/Gauss-Seidel relaxation, with the line sweep in the periodic ϕ-direction.

For the present problem, the second-order-accurate spatial discretization offers accurate solutions on medium-sized grids, such as the 64×64 grid used here. The discretization error of the first-order scheme is still too large for the solution to be of practical use on such grids. The slower convergence of the second-order scheme is amply compensated by the higher accuracy. Part of this slow-down could be compensated by an exact linearization and the use of a cyclic block-pentadiagonal solver (Thomas et al., 1985), but this has not been done because of the increase in complexity of the code. Instead, an approximate linearization with the same structure as for a first-order scheme has been used, with a modification to preserve the homogeneity of the equations.

A disadvantage of the present method is its memory requirement. The linearization of the M equations on the N-cell computational grid requires $5M^2N$ real numbers to be stored. The factor 5 is due to the 5-point stencil of our first-order discretization. In addition, $4M^2N$ real numbers are kept in memory to enable an acceleration of repeated line-inversions (see Appendix III). For two-dimensional problems, these storage requirements are still manageable. Extension of the method in its present form to three dimensions is not advisable. In principle, the multigrid method can be reformulated in a non-linear form, known as Full Approximation Storage (Brandt, 1981). In combination with a relaxation scheme that only uses the local $M \times M$ block of the full linearization, substantial savings on storage can be made. Such a non-linear multigrid method would be more appropriate for three-dimensional problems, or more complicated equations like the Navier-Stokes equations. It can be used on vector-computers if pattern relaxation is applied (see Paper II). Then, the computation of the residual and its linearization, as well as the relaxation scheme are vectorizable.

5.2. *Disk galaxies*

The computer program described in this paper is well suited for the efficient computation of the quasi-steady gas flow in the potential of a barred galaxy. The numerical solutions can be used to model observations of neutral hydrogen, or material that belongs to, or correlates well with the gaseous components of a disk galaxy. Detailed modeling of a specific galaxy falls beyond the scope of the present paper. A global gasdynamical model for our own Galaxy will be presented in a subsequent paper.

To obtain a quasi-steady solution for the flow of isothermal gas in a weakly barred galaxy, a distinction has to be made between 2 types of solutions that are of fundamental difference. The Type I solution only has shocks inside co-rotation, resulting in a net inflow. The gas mainly concentrates in a ring at some distance from the centre. The inflow turns out to be very small. Also, the timescale for the exchange of angular momentum between the bar and the gas is very large. Thus, the galaxy can easily maintain its appearance during a Hubble time. The smallness of the net average inflow found in this paper, indicates that its actual value is likely to be determined by the large-scale effects of processes not considered here, such as shear, bulk and turbulent viscosity, star formation, supernovae, infall of intergalactic matter, etc.

Many regular spiral galaxies must be of this Type I. Because star formation can be related to regions behind the shocks, most of the young and brightest stars will be found inside the co-rotation radius. The optical image of this type of galaxy will probably not extend beyond that radius. However, the neutral-hydrogen extent may be much larger (cf. Rogstad et al., 1974).

The Type II solution has shocks inside and outside co-rotation. As the shocks pump in opposite directions, the first inward and the second outward, the region around co-rotation will be depleted. Two rings form at the end of the shocks, one at some distance within the ILR for the shocks inside CR, and one at some distance outside the OLR for the shocks outside CR. In this case a steady state can be forced by creation of mass in depleted regions and annihilation in high-density areas. In reality, such a situation will tend to result in a galaxy with two distinct rings, like the type obtained by the particle simulations of Schwarz (1981), albeit that the latter results on a too short timescale for this process (van Albada, 1985). The main observable characteristics of a Type II galaxy, as compared to a Type I, are the shocks on the outside of the arms outside CR and the outer ring (not to be confused with the ringlike structures caused by spiral arms of small pitch angle). It would be interesting to find out if galaxies of this type exist.

Although the present study was not intended to cast new light on the subject of the origin and persistance of spiral structure, a few remarks are appropriate. Possible driving mechanisms for spiral arms are density waves, a stellar bar, a companion galaxy, and self-propagating stochastic star formation. The third option cannot explain spiral structure in isolated disk galaxies, and the fourth mechanism is not able to produce a regular large-scale pattern. Here we have chosen to generate spiral structure by means of a stellar bar. The weak bar used for the computation of Fig. 9 will be hard to recognize in the stellar distribution and is barely revealed in the gaseous component. A galaxy of this type would probably be classified as non-barred. On the other hand, the similarity between the present results and the spiral arms obtained by a driving density wave (e.g. Visser, 1980), makes one wonder if a unambiguous distinction can be made between a weak bar and a spiral density wave as the driving mechanism.

The bar-driven spiral pattern is characterized by large non-circular motions. The overall flow pattern is roughly elliptical. The long axis of the streamline-ellipses points in the y-direction near the centre of the galaxy, rotates over 90° at the ILR, and again at the OLR. As a consequence, the tilted-ring model for the observed neutral-hydrogen velocity field in disk galaxies may be just as well interpreted as a rotated-ellipse model.

The large non-circular motions also affect the rotation curves as determined from neutral-hydrogen observations of edge-on galaxies. Figure 10 demonstrates how misleading an interpretation on the basis of circular motions can be. If one compares the figures at $\phi_{obs} = 0°$ and $\phi_{obs} = 90°$, neglects the lightest gray-level and concentrates on the radii below $R_{CR} = 8.36$ – the "active" region of a Type I galaxy – the figure at 0° would provide a fairly flat rotation curve, whereas the figure at 90° has a slowly rising one. Apart from the central ring, the latter almost suggests rigid-body rotation. Arguments by Kormendy et al. (1979) that link observed properties of rotation curves with possible driving mechanisms for spiral structure thereby become less convincing, despite the obvious importance of such studies.

Acknowledgements. The author is indebted to B. van Leer for many clarifying and stimulating discussions. Part of this project was carried out at ICASE, NASA Langley Research Center, Hampton, Virginia, under financial support of the Netherlands Organization for the Advancement of Pure Research (Z.W.O.).

Appendix I
Interpolation of the state quantities for second-order accuracy

As mentioned in Sect. 3.1, a second-order-accurate spatial discretization can be obtained by a linear interpolation from the average state quantities in a cell to the average values at the boundary of a cell. The natural variables for this interpolation are the characteristic variables. For the present problem, the characteristic variables for the R-direction are

$$q^R=\begin{pmatrix}\ln\varrho+u/c\\ v/c\\ \ln\varrho-u/c\end{pmatrix}, \tag{A 1a}$$

and for the ϕ-direction

$$q^\phi=\begin{pmatrix}\ln\varrho+v/c\\ u/c\\ \ln\varrho-v/c\end{pmatrix}. \tag{A 1b}$$

Note that a different set of quantities is used for either direction. In general, these variables are obtained through the diagonalization of the Jacobian of the flux with respect to the conserved state quantities, i.e., $\frac{\partial f}{\partial w}$ and $\frac{\partial g}{\partial w}$ respectively. For the non-isothermal Euler equations we refer to Warming et al. (1975).

The numerical interpolation requires the differences across cell boundaries. For the R-direction we adopt

$$\begin{aligned}
q^R_{1,i,j+1}-q^R_{1,i,j}&=\frac{(\varrho_{i,j+1}-\varrho_{i,j})}{\frac{1}{2}(\varrho_{i,j+1}+\varrho_{i,j})}+(u_{i,j+1}-u_{i,j})/c\,,\\
q^R_{2,i,j+1}-q^R_{2,i,j}&=(\tilde v_{i,j+1}-\tilde v_{i,j})/c\,,\\
q^R_{3,i,j+1}-q^R_{3,i,j}&=\frac{(\varrho_{i,j+1}-\varrho_{i,j})}{\frac{1}{2}(\varrho_{i,j+1}+\varrho_{i,j})}-(u_{i,j+1}-u_{i,j})/c\,.
\end{aligned} \tag{A 2}$$

Here we have used the quantities

$$\varrho_{ij}=w_{1ij}/R_j,\quad u_{ij}=w_{2ij}/w_{1ij},\quad\text{and}\quad v_{ij}=w_{3ij}/w_{1ij}, \tag{A 3}$$

whereas

$$\tilde v_{ij}=v_{ij}-v_{Cj},\quad\text{with}\quad v_{Cj}=\frac{1}{R_j\Delta_j R}\int_{R_{j-\frac12}}^{R_{j+\frac12}}dR\,Rv_c(R)$$

and

$$v_c=(\omega_0(R)-\omega)R\,. \tag{A 4}$$

After averaging by (38) the vector $\overline{\Delta_R q^R}$ is transformed to the average differences of ϱ, u, and $\tilde v$ by

$$\begin{aligned}
(\overline{\Delta_R\varrho})_{ij}&=\tfrac12\varrho_{ij}\{(\overline{\Delta_R q^R_1})_{ij}+(\overline{\Delta_R q^R_3})_{ij}\}\,,\\
(\overline{\Delta_R u})_{ij}&=\tfrac12 c\{(\overline{\Delta_R q^R_1})_{ij}-(\overline{\Delta_R q^R_3})_{ij}\}\,,\\
(\overline{\Delta_R\tilde v})_{ij}&=c(\overline{\Delta_R q^R_2})_{ij}\,.
\end{aligned} \tag{A 5}$$

For the ϕ-direction similar expressions arise. Finally, the state quantities at the cell-boundary follow by

$$\begin{aligned}
w^+_{1,i,j+\frac12}&=R_{j+\frac12}\{\varrho_{ij}+\tfrac12(\overline{\Delta_R\varrho})_{ij}\}\,,\\
w^+_{2,i,j+\frac12}&=w^+_{1,i,j+\frac12}\{u_{ij}+\tfrac12(\overline{\Delta_R u})_{ij}\}\,,\\
w^+_{3,i,j+\frac12}&=w^+_{1,i,j+\frac12}\{\tilde v_{ij}+\tfrac12(\overline{\Delta_R\tilde v})_{ij}+v_c(R_{j+\frac12})\}\,,
\end{aligned} \tag{A 6}$$

and likewise for the other three boundaries. The interpolation of v_c in the R-direction is carried out explicitly, outside the limiting-averaging procedure. In this way a more accurate result is obtained than if v_{ij} would be used for the interpolation. The quantities u_{ij} and $\tilde v_{ij}$ are now of the same order of magnitude, and both are generally much smaller than v_c. Note that in the axisymmetric case the analytical solution (13) is an exact solution of the numerical equations. The same property is obtained for a first-order-accurate scheme if such a scheme is constructed by setting the average differences $\overline{\Delta_R\varrho}$ etc. in Eq. (A 6) to zero.

We end this appendix with the determination of ε_ϕ and ε_R as used in Eq. (38). We would like to avoid the effect of the limiter in smooth regions of the flow. This can be accomplished by taking ε_ϕ equal to the average of the differences in q^ϕ over a smooth part of the flow. As shocks occur at one-dimensional subsets of the computational domain, the L_1-norm of the differences in q^ϕ per ring j gives a good estimate:

$$\varepsilon_{\phi j}=\frac{1}{3N_\phi}\sum_{i=1}^{N_\phi}\sum_{k=1}^{3}|q^\phi_{k,i+1,j}-q^\phi_{k,i,j}|\,, \tag{A 7a}$$

where it is understood that i is periodic, so the values at $i=N_\phi+1$ are equal to those at $i=1$. In smooth regions the differences in q_k are of the order $\Delta\phi$, whereas the difference across a shock will be of order unity. The latter, however, occurs only in a few cells and is brought to order $O(1/N_\phi)=O(\Delta\phi)$ by the normalization. In the R-direction the situation is less straightforward, since a shock may occur along a large part of the ring j. We therefore adopt

$$\begin{aligned}
\varepsilon_{Rj}=\frac{1}{3N_\phi}\sum_{i=1}^{N_\phi}\sum_{k=1}^{3}\min(&|q^R_{k,i,j+1}-q^R_{k,i,j}|,\\
&|q^R_{k,i,j}-q^R_{k,i,j-1}|)\,,
\end{aligned} \tag{A 7b}$$

Some smoothing over 3 rings with weights $\frac14,\frac12,\frac14$ is performed afterwards.

Appendix II
Linearization of the residual

In the description of multigrid relaxation (Sect. 3.3), it has been assumed that the residual is of the form (45) and can be easily linearized. This is true for a first-order scheme. For a second-order scheme, however, the residual is computed on a 9-point stencil:

$$\begin{aligned}
r^n_{ij}=r(&w^n_{i,j-2},w^n_{i,j-1},w^n_{i-2,j},w^n_{i-1,j},w^n_{i,j},\\
&w^n_{i+1,j},w^n_{i+2,j},w^n_{i,j+1},w^n_{i,j+2})\,.
\end{aligned} \tag{A 8}$$

Instead of taking the Jacobian of the above expressions with respect to all its arguments, we will adopt an approximate linearization that has the same structure as the linearization of the first-order scheme and still preserves the homogeneity of the equations.

First consider the source term s, as given by Eq. (2). Its Jacobian is

$$\frac{\partial s}{\partial w}=\begin{pmatrix}0 & 0 & 0\\ -\dfrac{\partial V}{\partial R}+\omega^2R+\dfrac{c^2}{R}-\dfrac{v}{R} & 0 & 2\left(\dfrac{v}{R}+\omega\right)\\ -\dfrac{1}{R}\dfrac{\partial V}{\partial\phi}+\dfrac{uv}{R} & -\left(\dfrac{v}{R}+2\omega\right) & -\dfrac{u}{R}\end{pmatrix}, \tag{A 9}$$

no matter if the scheme is first- or second-order-accurate. The source term is homogeneous of degree one:

$$s=\left(\frac{\partial s}{\partial w}\right)w. \tag{A 10}$$

In the numerical scheme s is evaluated with the cell-averaged values w_{kij} and the derived quantities given by Eq. (A 3).

Now consider the flux in the R-direction. If f in Eq. (2) is differentiated to w, we obtain

$$\frac{\partial f}{\partial w}=\begin{pmatrix}0 & 1 & 0\\ c^2-u^2 & 2u & 0\\ -uv & v & u\end{pmatrix}. \tag{A 11}$$

The full flux is a homogeneous function of the degree one:

$$f=\left(\frac{\partial f}{\partial w}\right)w. \tag{A 12}$$

Contrary to the source-term, the numerical flux is computed from values at the cell-boundary, so Eq. (A 6) has to be used during the differentiation. To simplify the notation, we denote the values at the boundary by an asterisk and drop all the subscripts, so Eq. (A 6) becomes

$$\begin{aligned}w_1^*&=R^*(w_1/R+\tfrac{1}{2}\overline{\Delta_R\varrho}),\\ w_2^*&=w_1^*(w_2/w_1+\tfrac{1}{2}\overline{\Delta_R u}),\\ w_3^*&=w_1^*(w_3/w_1+\tfrac{1}{2}\overline{\Delta_R v}+v_c^*-v_C),\end{aligned} \tag{A 13}$$

and similarly for the other three cell boundaries. In a first-order scheme the average differences $\overline{\Delta_R\varrho}$ etc. are zero. To give the second-order linearization the same structure as the first-order one, we neglect the dependence on w of these average differences. The derivative of the full flux f^* now becomes

$$\frac{\partial f^*}{\partial w}=w_1^*/w_1\begin{pmatrix}u^*-u(\varrho/\varrho^*) & 1 & 0\\ (u^{*2}+c^2)(\varrho/\varrho^*)-2uu^* & 2u^* & 0\\ u^*(v^*-v)-uv^*(\varrho/\varrho^*) & v^* & u^*\end{pmatrix}. \tag{A 14}$$

This expression does not have the property of homogeneity. However, if Eq. (A 14) is replaced by

$$\frac{\partial f^*}{\partial w}=w_1^*/w_1\begin{pmatrix}u^*-u & 1 & 0\\ (u^{*2}+c^2)-2uu^* & 2u^* & 0\\ u^*(v^*-v)-uv^* & v^* & u^*\end{pmatrix}, \tag{A 15}$$

we again obtain $f^*=\left(\frac{\partial f^*}{\partial w}\right)w$. Thus, Eq. (A 15) is used for the linearization of the full flux f^*, regardless whether the scheme is first- or second-order-accurate.

For the split fluxes $f^{\pm}$ and full and split fluxes g and $g^{\pm}$ in the ϕ-direction the same type of linearization is applied. We only give the result for $f^{\pm}$:

$$f^{\pm *}=\frac{w_1^*}{\pm 4c}(u^*\pm c)^2\begin{pmatrix}1\\ \pm 2c\\ v^*\end{pmatrix}, \tag{A 16a}$$

$$\frac{\partial f^{\pm *}}{\partial w}=w_1^*/w_1\begin{pmatrix}(u^*\pm c)(u^*\pm c-2u)/(\pm 4c) & (u^*\pm c)/(\pm 2c) & 0\\ \tfrac{1}{2}(u^*\pm c)(u^*\pm c-2u) & u^*\pm c & 0\\ (u^*\pm c)\{(u^*\pm c)(v^*-v)-2uv^*\} & v^*(u^*\pm c)/(\pm 2c) & (u^*\pm c)^2/(\pm 4c)\end{pmatrix}. \tag{A 16b}$$

Again $f^{\pm *}=\left(\frac{\partial f^{\pm *}}{\partial w}\right)w$.

Finally, we remark that the matrix M, as given in Eq. (44b), and the right-hand side $f=r^n$ (not to be confused with the flux) are now related according to $r^n=M^nw^n$, both for the first- and second-order-accurate scheme.

Appendix III
A cyclic block-tridiagonal inversion

For a first-order scheme, and for the approximate linearization of our second-order scheme, the matrix L in Eq. (42) has one main-diagonal and 4 off-diagonals, where a diagonal-element is understood to be a 3×3 block. The blocks of the maindiagonal are denoted by A_{ij}^*, of the off-diagonals by B_{ij}^R, C_{ij}^R and B_{ij}^ϕ, C_{ij}^ϕ, according to

$$\begin{aligned}&A_{ij}^*=\sigma_{ij}I-A_{ij},\quad A_{ij}=\left(\frac{\partial r_{ij}}{\partial w_{ij}}\right),\\ &B_{ij}^R=\left(\frac{\partial r_{ij}}{\partial w_{i,j-1}}\right),\quad C_{ij}^R=\left(\frac{\partial r_{ij}}{\partial w_{i,j+1}}\right),\\ &B_{ij}^\phi=\left(\frac{\partial r_{ij}}{\partial w_{i-1,j}}\right),\quad C_{ij}^\phi=\left(\frac{\partial r_{ij}}{\partial w_{i+1,j}}\right).\end{aligned} \tag{A 17}$$

A line-sweep at ring j requires the inversion of the cyclic block-tridiagonal matrix

$$K_j=\begin{pmatrix}A_{1j}^* & -C_{1j} & 0 & \dots & 0 & -B_{1j}\\ -B_{2j} & A_{2j}^* & -C_{2j} & \dots & 0 & 0\\ \vdots & \vdots & \vdots & & \vdots & \vdots\\ 0 & 0 & 0 & \dots & A_{N-1,j}^* & -C_{N-1,j}\\ -C_{N,j} & 0 & 0 & \dots & -B_{N,j} & A_{N,j}^*\end{pmatrix}. \tag{A 18}$$

Here the superscript ϕ for B_{ij} and C_{ij} has been dropped, and the same symbol is left out for N_ϕ. The inversion of K_j for the non-cyclic case (i.e., $B_{1j}=0$ and $C_{Nj}=0$) is standard. It is carried out by the decomposition of K_j in a lower and upper block-bidiagonal matrix, $K=K_lK_u$, which directly yield the solution of $Ks=f$ through $K_lg=f$ and $K_us=g$, thus requiring two sweeps. The cyclic version requires an additional third sweep.

We now give the algorithm. The subscript j is omitted. The first, forward sweep is

$$\begin{aligned}&\alpha_1:=A_1,\quad D_1:=B_1,\quad \text{and}\quad g_1^*:=f_1;\\ &\beta_i:=B_i\alpha_{i-1}^{-1},\quad \alpha_i:=A_i-\beta_iC_{i-1},\quad D_i:=\beta_iD_{i-1},\end{aligned}$$

and

$$g_i^*:=f_i+\beta_ig_{i-1}^*\quad \text{for}\quad i=2,\dots,N. \tag{A 19}$$

The second, backward sweep is

$$\begin{aligned}&P_N:=\alpha_N^{-1}C_N,\quad Q_N:=\alpha_N^{-1}D_N,\quad \text{and}\quad s_N^*:=\alpha_N^{-1}g_N^*;\\ &P_i:=(\alpha_i^{-1}C_i)P_{i+1},\quad Q_i:=(\alpha_i^{-1}C_i)Q_{i+1}+\alpha_i^{-1}D_i,\end{aligned}$$

and

$$s_i^*:=\alpha_i^{-1}[g_i+C_is_{i+1}^*]\quad \text{for}\quad i=N-1,\dots,1. \tag{A 20}$$

So far, s^* is computed as if the problem was non-cyclic. To obtain the final cyclic solution, we have to solve the linear system

$$\begin{pmatrix} (I-P_1) & -Q_1 \\ -P_N & (I-Q_N) \end{pmatrix} \begin{pmatrix} s_1 \\ s_N \end{pmatrix} = \begin{pmatrix} s_1^* \\ s_N^* \end{pmatrix}, \tag{A 21}$$

which yields the correct values of s at $i=1$ and $i=N$. Finally, a third sweep is performed to correct for the periodicity:

$$s_i = s_i^* + P_i s_1 + Q_i s_N, \quad \text{for} \quad i=1,\ldots,N. \tag{A 22}$$

For the SLGS-scheme, this solution is subtracted from f_{ij} by using Eq. (46). Note that for a given j this affects f_{ij} in the rings $j-1$, j, and $j+1$.

As these cyclic tridiagonal inversions have to be carried out with identical blocks 2 times during one SLGS-step, 4 times in a full multigrid V-cycle and even more times when the linearization is frozen, it is useful to store the blocks α_{ij}^{-1}, β_{ij}, P_{ij}, and Q_{ij} in memory. In this way, a repeated line-inversion only involves multiplications of vectors by blocks. The multiplications of blocks by blocks and the inversion of α_{ij} is avoided. This saves a substantial amount of cpu-time.

References

Berman, R.H., Pollard, D.J., Hockney, R.W.: 1979, *Astron. Astrophys.* **78**, 133

Boris, J.P., Book, D.L.: 1973, *J. Comput. Phys.* **11**, 38

Bosma, A.: 1981a, *Astron. J.* **86**, 1791

Bosma, A.: 1981b, *Astron. J.* **86**, 1825

Brandt, A.: 1981, in *Lecture Notes in Mathematics* **960**, 220

Burstein, D., Rubin, V.C., Thonnard, N., Ford, W.K.: 1982, *Astrophys. J.* **253**, 70

Collela, P., Woodward, P.R.: 1984, *J. Comput. Phys.* **54**, 174

Contopoulos, G.: 1980, *Astron. Astrophys.* **81**, 198

Fujimoto, M.: 1968, in *Nonstable Phenomena in Galaxies*, IAU *Symp.* **29**, ed. M. Arakeljan, Armenian Academy of Science, Yerevan, p. 453

Godunov, S.K.: 1959, *Mat. Sb.* **47**, 271 (see *Cornell Aeronautical Lab. Transl.*)

Hackbusch, W.: 1981, in *Lecture Notes in Mathematics* **960**, 177

Harten, A., Lax, P.D., van Leer, B.: 1983, *SIAM Review* **25**, 35

Huntley, J.M.: 1980, *Astrophys. J.* **238**, 524

Isaacman, R.B.: 1981, *Astron. Astrophys.* **95**, 46

Jameson, A.: 1983, *Appl. Math. Comput.* **13**, 327

Kormendy, J., Norman, C.A.: 1979, *Astrophys. J.* **233**, 539

Kormendy, J.: 1982, in *Morphology and Dynamics of Galaxies*, eds. L. Martinet, M. Mayor, p. 113

Miller, R.H., Smith, B.F.: 1979, *Astrophys. J.* **227**, 785

Mulder, W.A., Hooimeyer, J.R.A.: 1984, *Astron. Astrophys.* **134**, 158 (Paper IV)

Mulder, W.A.: 1985a, in *Lecture Notes in Physics* **218**, 417

Mulder, W.A., van Leer, B.: 1985, *J. Comput. Phys.* **59**, 232 (Paper I)

Mulder, W.A.: 1985b, *J. Comput. Phys.* **60**, 235 (Paper III)

Osher, S., Chakravarty, S.: 1983, *J. Comput. Phys.* **50**, 447

Pfenniger, D.: 1984, *Astron. Astrophys.* **141**, 171

Roberts, W.W.: 1969, *Astrophys. J.* **158**, 123

Roberts, W.W., Shu, F.H.: 1972, *Astrophys. Letters* **12**, 49

Roberts, W.W., Huntley, J.M., van Albada, G.D.: 1979, *Astrophys. J.* **233**, 67

Roe, P.L.: 1981, *J. Comput. Phys.* **43**, 357

Rogstad, D.H., Lockhart, I.A., Wright, M.C.H.: 1974, *Astrophys. J.* **193**, 309

Rubin, V.C., Ford, W.K., Thonnard, N.: 1982, *Astrophys. J.* **261**, 439

Sandage, A.J.: 1961, *The Hubble Atlas of Galaxies*, Carnegie Institution of Washington

Sanders, R.H., Lowinger, T.: 1972, *Astron. J.* **77**, 292

Sanders, R.H., Prendergast, K.H.: 1974, *Astrophys. J.* **188**, 489

Sanders, R.H., Huntley, J.M.: 1976, *Astrophys. J.* **209**, 53

Sanders, R.H., Tubbs, A.D.: 1980, *Astrophys. J.* **235**, 803

Schempp, W.V.: 1982, *Astrophys. J.* **258**, 96

Schwarz, M.P.: 1981, *Astrophys. J.* **247**, 77

Sellwood, J.A.: 1981, *Astron. Astrophys.* **99**, 362

Shu, F.H., Milione, V., Gebel, W., Yuan, C., Goldsmith, D.W., Roberts, W.W.: 1972, *Astrophys. J.* **173**, 557

Sørensen, S.A., Matsuda, T., Fujimoto, M.: 1976, *Astrophys. Space Sci.* **43**, 491

Sørensen, S.A., Matsuda, T.: 1982, *Monthly Notices Roy. Astron. Soc.* **198**, 865

Steger, J.L., Warming, R.F.: 1981, *J. Comput. Phys.* **40**, 263

Thomas, J.L., van Leer, B., Walters, R.W.: 1985, AIAA paper no. 85-1680, AIAA 18th Fluid Dynamics, Plasma Dynamics and Lasers Conference, Cincinnati, Ohio

van Albada, G.D., Roberts, W.W.: 1981, *Astrophys. J.* **246**, 740

van Albada, G.D., van Leer, B., Roberts, W.W.: 1982, *Astron. Astrophys.* **108**, 76

van Albada, G.D.: 1985, *Astron. Astrophys.* **142**, 491

van Leer, B.: 1977, *J. Comput. Phys.* **23**, 276

van Leer, B.: 1979, *J. Comput. Phys.* **32**, 101

van Leer, B.: 1982, in *Lecture Notes in Physics* **170**, 507

van Leer, B., Mulder, W.A.: 1985, in *Numerical Methods for the Euler Equations of Fluid Dynamics*, eds. F. Angrand, A. Dervieux, J.A. Desideri, and R. Glowinski, SIAM, Philadelphia, p. 312

van Leer, B.: 1985, in *Large-Scale Computations in Fluid Mechanics*, *Lectures in Applied Math.* **22**, eds. B.E. Engquist, S. Osher, R.C.J. Somerville, American Math. Soc., Providence, Rhode Island, p. 327

Visser, H.C.D.: 1980, *Astron. Astrophys.* **88**, 159

Warming, R.F., Beam, R.M., Hyett, B.J.: 1975, *Math. Comput.* **29**, 1037

Woodward, P.R.: 1975, *Astrophys. J.* **195**, 61

Woodward, P.R., Collela, P.: 1984, *J. Comput. Phys.* **54**, 115